Production of Neutral Strange Hadrons with High Transverse Momentum in Pb+Pb Collisions at 158A GeV

Tim Schuster
Institut für Kernphysik

Diplomarbeit
vorgelegt beim Fachbereich Physik
der Johann Wolfgang Goethe-Universität
Frankfurt am Main

Februar 2006

Zusammenfassung

In dieser Arbeit wird die *Produktion seltsamer neutraler Teilchen mit hohen Transversalimpulsen in Pb+Pb Reaktionen bei 158A GeV* untersucht. Diese Analyse basiert auf Daten, die mit dem Experiment NA49 am europäischen Teilchenlabor CERN aufgenommen wurden.

Das *Standardmodell der grundlegenden Teilchen und Kräfte* stellt den heutigen Stand der Suche nach den Grundbausteinen der Natur dar. Neben den *Leptonen* sind darin *Quarks* als Elementarteilchen dargestellt. Ausser diesen Teilchen kennt das Standardmodell vier grundlegende Kräfte: Die starke, elektromagnetische und die schwache Wechselwirkung werden im Standardmodell durch Quanten-Feldtheorien beschrieben, d.h. sie wirken durch den Austausch von *Vektorbosonen*. Die vierte Kraft, die Gravitation, wirft noch Fragen auf. Im Gegensatz zu den Leptonen kommen Quarks in der Regel nicht einzeln vor, sondern nur in gebundenen Zuständen, den *Hadronen*. Das liegt an den Besonderheiten der Kraft, die zwischen den Quarks wirkt: der starken Wechselwirkung. Sie ist die einzige unter den vier Kräften, deren Stärke nicht mit dem Abstand abnimmt. Das liegt daran, dass ihre Austauschteilchen, die *Gluonen*, selber eine Ladung tragen und damit selbst der starken Wechselwirkung unterliegen. Dies führt zum Einschluss der Quarks in Hadronen, dem *confinement*.

Die relativistische Schwerionenphysik befasst sich mit der Suche nach einem neuen Zustand hadronischer Materie, dem Quark-Gluon-Plasma. Man geht heute davon aus, dass dieser Zustand am Anfang unseres Universums bestand, bis etwa 10^{-5} s nach dem Urknall, als Dichte und Temperatur des Universums so groß waren, dass Hadronen keinen Bestand haben konnten und sich statt dessen Quarks und Gluonen frei bewegen konnten. Die Hadronen die sich nach der Abkühlung dieses Zustandes bildeten, haben im Wesentlichen bis heute, 12 Milliarden Jahre nach dem Urknall Bestand. Nur im Inneren von Neutronensternen erwarten Physiker eine Dichte die so hoch ist, dass die

Neutronen überlappen und ein Quark-Gluon-Plasma bilden.

Eine Möglichkeit, diesen Zustand experimentell zu untersuchen, bieten Schwerionenkollisionen bei hoch-relativistischen Energien. Dazu werden z.B. im Beschleuniger SPS am CERN Bleikerne auf eine Energie von $158A$ GeV gebracht. Die von verschiedenen Experimenten dieses SPS-Schwerionenprogramms 2000 verkündete Entdeckung eines neuen Materiezustandes basierte auf einer Vielzahl von Messwerten, die ein Gesamtbild des Quark-Gluon-Plasma zeichneten. Später durchgeführte Experimente bei höheren Energien am RHIC-Beschleuniger brachten andere Observable ins Spiel, die dieses Bild ergänzen können. Die meisten in Schwerionenkollisionen produzierten Hadronen stammen aus Stößen mit geringem Impulsübertrag und weisen deshalb einen Transversalimpuls (senkrecht zur ursprünglichen Strahlrichtung) von $p_{\mathrm{T}} < 1.5$ GeV/c auf. Für den Bereich höherer Transversalimpulse kommen verschiedene Mechanismen zur Hadronisierung in Frage. Ein am RHIC beobachtetes Ansteigen der Verhältnisse von Baryonen zu Mesonen wird als Anzeichen für Hadronisierung durch Rekombination von Quarks erklärt.

Das Experiment NA49 wurde dafür konzipiert, den hadronischen Endzustand von Schwerionenkollisionen zu untersuchen. Es hat eine große Akzeptanz, die es ermöglicht etwa 70% der tausenden von geladenen Teilchen, die in jeder Kollision entstehen, zu vermessen. Neutrale seltsame Teilchen, wie die in der vorliegenden Arbeit untersuchten $\mathrm{K}^0_{\mathrm{S}}$ und Λ werden über ihren schwachen Zerfall in zwei geladene Teilchen identifiziert. Die V-Form der Tochterspuren gibt ihnen den Namen V^0-Teilchen. Die Analyse beruht auf der Rekonstruktion der invarianten Masse der V^0-Teilchen in einzelnen Bereichen des Phasenraums aus den Zerfallsprodukten. Die Reichweite in p_{T} für diese Methode ist nur durch die statistische Häufigkeit, die mit p_{T} stark abnimmt, beschränkt.

Ein wichtiger Bestandteil dieser Analyse ist es, die Menge der V^0-Kandidaten durch geeignete Kriterien ("cuts") so einzugrenzen, dass falsche Kombinationen unterdrückt werden. Gleichzeitig muss darauf geachtet werden, durch diese cuts das Signal so wenig wie möglich zu treffen. Der Anteil der Teilchen, die wegen der geometrischen Akzeptanz des Experiments oder durch Ineffizienzen in der Analyse nicht gemessen wurden, wird durch eine Simulation ermittelt. Daraus werden für jeden Bereich des Phasenraums Korrekturfaktoren ermittelt, um die gemessenen Rohwerte in korrigierte Spektren umzurechnen. Das aus diesen korrigierten Spektren berechnete Verhältnis $\mathrm{K}^0_{\mathrm{S}}/\Lambda$ gleicht qualitativ den Messungen am RHIC und bestärkt die anderen Hinweise darauf, dass bei den höchsten am SPS verfügbaren Energien ein Quark-Gluon-Plasma erreicht wird.

Erklärung

Ich versichere hiermit, dass ich die vorliegende Arbeit selbständig verfasst, keine anderen als die angegebenen Hilfsmittel verwendet und sämtliche Stellen, die benutzten Werken im Wortlaut oder dem Sinne nach entnommen sind, mit Quellen- bzw. Herkunftsangaben kenntlich gemacht habe.

Frankfurt am Main, den 28. Februar 2005

Tim Schuster

Acknowledgements

First of all, I would like to thank my supervisor Christoph Blume for giving me the opportunity to work on this interesting topic. And thank you for your continuous and comprehensive support throughout my work. Let me also acknowledge Marek Gaździcki's enthusiasm that he shared just like his knowledge. His ideas and explanations always helped me to advance in the analysis and in understanding the topic. Herbert Ströbele likewise provided valuable suggestions and knowledge to my analysis. Reinhard Stock has sparked my interest in heavy ion physics through his lecture. I am indebted to him for conveying his enthusiasm about many topics.

I owe a great deal to Karolin and Subin; not only for proof-reading this thesis but also for your great friendship. I am also very grateful to Dani and Robert for their support. I feel lucky to have shared not only the course of my studies with you and Dominik Heide, Dominique Akoury, Irina Sagert, Peter Döring, Jan Hoffmann, Manuela Otto, Tim Rienecker, Bernd Sicherl and Christoph Wiesner. Let me thank you all for the good time.

I am indebted to Peter Dinkelaker for introducing me to the group in Frankfurt, and into the working methods and basic concepts of heavy ion physics. I am glad I shared an office with you and want to thank you for many actions and discussions.

I am fortunate to share the work at the IKF with Christopher Alt, Werner Amend, Jutta Berschin, Matthias Hartig, Stefan Kniege, Michael Kliemant, Uli Köpf, Thorsten Kollegger, Fred Kramer, Benjamin Lungwitz, Michael Mitrovski, Matheusz Płoskoń, Rainer Renfordt, Wolfgang Sommer and Claudia Strabel who all contribute in their way to the working conditions and the friendly atmosphere at the IKF. Thanks to all of you and to Heidrun Rheinfels-Immanns, Roland Bramm, Dominik Flierl and Thomas Dietel for discussions about physics and other topics as well as valuable help in many circumstances.

This analysis would not be possible without the great efforts made by members of the NA49 collaboration throughout the existence of this experiment. I am impressed by the friendly working atmosphere prevailing within the collaboration and want to thank in particular Peter Seyboth for providing suggestions for this analysis. Furthermore, I also highly appreciate working and discussing with András László.

I am grateful to Andres Sandoval and Latchezar Betev for their support during my time at CERN. In this context, I also want to thank Björn Rudde for inspiring discussions and several diversions.

I am very thankful for the support and encouragement I receive from my family in all circumstances. It is the indispensible basis for all I have reached.

And finally thank you, Janina for—everything.

Contents

1 Introduction **3**

1.1 The Standard Model of Fundamental Particles and Interactions 3

1.2 Strangeness and V^0 Particles 4

1.3 Hadrons, the Strong Interaction and Confinement 6

2 The Search for the Quark-Gluon Plasma **9**

2.1 Quark-Gluon Plasma in the Universe 9

2.2 Quark-Gluon Plasma in the Laboratory 10

3 The NA49 Experiment **15**

3.1 Particle Accelerators at CERN 15

3.2 Detector Concept 17

3.3 The Time Projection Chambers 20

3.4 Data Flow 22

4 Data Processing in NA49 **27**

4.1 Hardware Resources at CERN 27

4.2 Reconstruction Chain 29

4.3 The Analysis Framework ROOT 37

4.4 Simulation Chain 39

5 V^0 Analysis up to High p_T **43**

5.1 Dataset and Event Cuts 43

5.2 Analysis Cuts 45

5.3 Signal Extraction 50

5.4 Acceptance and Efficiency Correction 55

5.5 Cut Studies for K^0_S 56

5.6 Cut Studies for Λ 60

5.7 Open Issues 64

6 Results and Discussion **69**

7 Summary **73**

A Additional Figures **a**

B Relativistic Kinematics **i**

C List of Used Abbreviations **m**

Bibliography **o**

Chapter 1

Introduction

Are there basic constituents making up our world, and if they exist, what is their nature? The concept of elementary particles has been used many times by scientists in the ambition to understand and explain nature. In the ancient world, the idea of a basic entity that cannot be dismantled—the atom—was based upon philosophical considerations. The understanding of this aspect has evolved together with experiments conducted from the 19th century onwards, in which not only the atom per se was revealed, but also found to be composed of subatomic particles again.

1.1 The Standard Model of Fundamental Particles and Interactions

The current status of the quest for elementary particles is summarised in the *Standard Model of Fundamental Particles and Interactions* [1]. According to the model, the basic components of matter are *leptons* and *quarks*. They are held together by four basic forces. Thereof the weak, the electromagnetic and the strong force can be described in terms of gauge theories and are understood to be mediated by the *gauge bosons*. The standard model was able to predict the existence and properties of some particles prior to their observation. A great success was the confirmation of assertions about the W and Z boson masses and their decay channels through measurements. A remaining challenge to the standard model is to explain the origin of particles' masses and the fourth fundamental force, gravitation. The Higgs boson postulated in this context still awaits experimental discovery.

Table 1.1 gives an overview of the elementary particles. The leptons don't have any internal structure and thus can be observed individually. They are subject to the weak force, and the charged ones also to the electromagnetic interaction. Having a spin of 1/2, leptons—like quarks—are fermions. The quarks, in addition to weak and electromagnetic, also react on the strong interaction. This force confines them into *hadrons*. Two classes of hadrons are known: *mesons* made up of $q\ \overline{q}$ pairs and *baryons* characterised by $q\ q\ q$ combinations. Whether pentaquark ($q\ q\ q\ q\ \overline{q}$) or even larger baryons exist is still being debated.

Leptons			Charge
ν_{e}	ν_μ	ν_τ	0
e	μ	τ	-1
Quarks			
u	c	t	2/3
d	s	b	$-1/3$

Table 1.1: The three generations of leptons and quarks, the basic constituents of matter.

Quantum field theories describe the forces in the standard model. Their overview is given in Table 1.2. Quantum-Electrodynamics (QED) describes the electromagnetic interaction via photon exchange. The unification of electromagnetic and weak interactions was achieved in the Glashow-Salam-Weinberg (GSW) theory. The strong interaction is formalised in the quantum theory of colour fields, Quantum-Chromodynamics (QCD). Future experiments are hoped to provide evidence for an integration of the three, the grand unified theory (GUT).

1.2 Strangeness and V^0 Particles

The objects of investigation in this thesis are *neutral strange hadrons* or, to be more precise: hadrons without electric charge, containing one strange or anti-strange quark. The hadronic matter familiar to us only consists of protons and neutrons that are made up of u and d quarks only. The s quark was the first new quark produced in experiments.

Interaction	strong	electromagnetic	weak	gravitation
Couples to	colour charge	electric charge	weak charge	mass
Range / m	$\approx 10^{-15}$	∞	$\approx 10^{-18}$	∞
Coupling constant	$\alpha_s \approx 1$ (large r) $\alpha_s < 1$ (small r)	$\alpha = 1/137$	$\approx 10^{-5}$	$\approx 10^{-37}$
Gauge boson	8 gluons (g)	photon (γ)	W^+, W^- and Z	

Table 1.2: The four basic interactions.

It appeared contained in new particles that had "strange" properties: Unstable particles observed so far had typical lifetimes of $\approx 10^{-24}$ s, but the strange particles lived $\approx 10^{-10}$ s. The cause is found in the difference of production and decay mechanisms. While the generation of strangeness happens via the strong interaction through simultaneous production of strange and anti-strange particles, their decay is based on a slower process: the weak interaction. The weak interaction is the only fundamental force that can to alter the flavour of a quark. This happens e.g. in the β-decay.

The first strange particle to be detected was the neutral meson K^0 in 1946. Being a neutral particle, it does not interact electromagnetically with the detector material. It was identified via its decay into two oppositely charged particles instead. The name V^0 particle was derived from the shape of the tracks left by the daughter particles and stands for all particles with this decay topology.

The K^0 and its antiparticle $\overline{K}^0$ are eigenstates of the strong interaction, whereas their decay is characterised by the weak interaction's eigenstates K^0_L and K^0_S. 50 % of both K^0 and $\overline{K}^0$ decay as K^0_L and the other half as K^0_S. The lifetimes of the two differ dramatically: While K^0_L ("L" for long) has a lifetime of $5 \cdot 10^{-8}$ s, K^0_S decays after $9 \cdot 10^{-11}$ s. Accessible for this analysis is only the K^0_S, that practically only decays into two pions. The K^0_L lives too long and thus decays after having passed the detector. The channel $K^0_S \to \pi^+\pi^-$ was used to identify the K^0_S.

Besides, the Λ baryon has been analysed here. It is the lightest of the *hyperons*, i.e. the baryons carrying strangeness. Like the K^0_S, it falls into the category of V^0 particles with its decay channel $\Lambda \to p\pi^-$. The branching ratio of the channels used to identify the particles has to be taken into account when interpreting the results.

1.3 Hadrons, the Strong Interaction and Confinement

Following the revelation of the inner structure of the nucleus, a whole new class of particles that appeared as elementary as the proton or the neutron was found in experiments with cosmic particles and accelerator beams. It started with the discovery of the pion in 1947, and by the 1960s, a whole "zoo" of hundreds of *hadrons* was observed—too many to be considered as elementary particles any more. In the same way as the periodic table of elements helped understanding that the different nuclei are built up of nucleons, the static quark model presented by Gell-Mann and Zweig in 1964 gave an ordering mechanism to this large amount of particles. All observed states could at that time be described as different compositions of quarks occuring in three different flavours: u, d, s and the corresponding antiquarks. This scale has been extended (and therewith concluded) to the six quark flavours present in the standard model (see Table 1.1). Observed baryons with three quarks in the same state (flavour, spin) seemed to violate the exclusion principle of Fermi-Dirac statistics that should actually be valid for all fermions. This problem was overcome through the introduction of a new quantum number: the colour charge.

The spatial resolution of an experiment is determined by the energy of the probe. Experiments in particle physics therefore could unscramble smaller systems along with the progress of accelerator development. Analogous to the Rutherford scattering experiment that revealed the nucleus inside the atom, deep inelastic e-p scattering experiments conducted in the 1970s affirmed the substructure of the nucleon. Three point-like objects were discovered within, and the predicted quark charges (see Table 1.1) confirmed. Another important test for the quark picture is the ratio of hadron to lepton production in e^+ e^- annihilation reactions at different energies. The measurement of this ratio confirmed the presence of three colour degrees of freedom for the quarks.

Although quarks underlie all fundamental forces, the strong interaction is by far dominant inside hadrons. QCD describes it as mediated by the exchange of gluons among colour charged particles. This is equivalent to the exchange of photons in QED. Both photons and gluons have no rest mass. But it makes a huge difference that while photons are electrically neutral, gluons carry colour charge, enabling them to interact with each other and themselves. This entails two extraordinary features of the strong interaction: *confinement* and *asymptotic freedom*.

Confinement denotes the fact that quarks cannot be observed alone but only confined into hadrons. The strong force binding them together does not decline with increasing separation of the quarks but stays constant. This is reflected in the $q\ \overline{q}$ potential

$$V = -\frac{4}{3}\frac{\alpha_s}{r} + k \cdot r$$

where α_s is the coupling constant of the strong interaction. The first term describes the exchange of one massless gluon which is the predominant effect at short distances making the potential Coulomb-like here. For larger distances, the potential rises linearly. As a consequence, an infinite amount of energy would be needed to completely separate the $q\ \overline{q}$ pair making up a meson. Before this can happen, the colour field between them has accumulated enough energy to produce a new $q\ \overline{q}$ pair. They form mesons with the quarks that were supposed to be separated. Again, only colour neutral objects are present.

Another feature of the strong interaction that has been discovered in deep inelastic scattering of electrons on protons is that quarks inside hadrons behave like free particles. This property called asymptotic freedom is reflected in the running coupling constant [2] of strong interaction. For small distances that are equivalent to high momentum transfers Q^2, the coupling constant vanishes:

$$\lim_{Q^2 \to \infty} \alpha_s\left(Q^2\right) = 0$$

In this large momentum transfer region, it is thus possible to construct a perturbation theory: perturbative QCD (pQCD) manages to describe jet production in high energy p+p collisions.

In the low momentum transfer region, where $\alpha_s = 1$, perturbation theories are not applicable, as higher order effects play an as important role as first-order effects. Here the most promising possibility to make predictions is lattice QCD. It uses an approximation of the continuous space-time by a discrete lattice to describe these processes. It requires huge computing power and still implies a number of technical problems. Nevertheless, it yields quantitative results like a good reproduction of the hadron masses and predictions for new phases of strongly interacting matter.

Chapter 2

The Search for the Quark-Gluon Plasma

Interaction among quarks cannot be studied directly, as they stay confined in hadrons. One of the indirect approaches is to probe the state of nuclear matter under different conditions and thus explore its phase diagram. From heating or compressing nuclei, the production of states different to the basic appearance are expected, and these phase transitions can reveal the nature of the underlying forces.

A phase transition to the *quark-gluon plasma* (QGP), where the constituents of strongly interacting matter can move freely in an extended volume, is of exceptional interest. Theory predicts this state to exist above a critical energy density. This condition can be achieved experimentally by colliding large nuclei at velocities close to the speed of light. Experiments have been conducted at various collision energies, and their results support the theoretical considerations.

2.1 Quark-Gluon Plasma in the Universe

Besides the motivation to understand the fundamental properties of strong interaction, the creation of a QGP in these experiments of *heavy ion physics* would reproduce the conditions that prevailed only fractions of seconds after the big bang on a small scale, and give physicists the possibility to glance at the beginning of our universe. While the big bang itself eludes description so far, attempts to explain the evolution of the universe reach back up to $\approx 10^{-40}$ s after it. The implication from the expansion of the

universe observed today is that the energy density rises when approaching the big bang. The latter is seen as a singularity where the energy density would be infinite. A QGP phase should though have existed from $\approx 10^{-37}$ s after the big bang onwards, eventually condensing into hadrons when the energy density drops below the critical value due to the expansion $\approx 10^{-5}$ s later.

Another natural appearance of matter composed of deconfined quarks and gluons is expected from the inside of neutron stars. These remnants of supernovae aggregate 1.4 times the solar mass within their radius of 5 km. The density following from this exceeds that of normal nuclear matter by far, causing the distance between nucleons to drop below their size. An extended region of overlapping nucleons, where quarks and gluons move freely, is thus anticipated in the centre of neutron stars.

2.2 Quark-Gluon Plasma in the Laboratory

In the more than 30 years of heavy ion physics, collisions at various energies have been studied. Interpretation of the data has evolved along with the development of experimental means. The challenge in trying to probe a QGP produced in a heavy ion collision is that this state can not be observed directly. It transforms back into hadronic matter after some fm/c. Afterwards, the energy density is still high enough to cause the produced particles to interact and thereby may distort the information about the partonic state.

History of Relativistic Heavy Ion Collision Physics

Heavy ion collisions at relativistic energies started in the 1970s with experiments at the Bevatron/Bevalac accelerator facility in Berkeley. When QCD started making predictions about the location of the phase transition, it was realised that higher energies were needed. Experimentalists moved from Berkeley to the Alternating Gradient Synchrotron AGS at the Brookhaven National Laboratory (BNL) and on to CERN's Super Proton Synchrotron (SPS). Here, a provisional highlight was reached in 2000, when in a common declaration of the different experiments [3] the discovery of "a new state of matter" was claimed.

While the earlier heavy ion experiments were conducted with accelerators that had

originally been designed for particle physics experiments with proton beams, the Relativistic Heavy Ion Collider RHIC located at the BNL was the first dedicated tool for heavy ion physics. With a rise in the centre-of-mass energy [1] $\sqrt{s_{\mathrm{NN}}}$ by an order of magnitude compared to SPS, new observables to probe the created matter arose from the measurements made at RHIC.

Up to now, heavy ion collisions in an energy range from 2.5 GeV $\leq \sqrt{s_{\mathrm{NN}}} \leq$ 200 GeV could be created and studied. At the advent of CERN's Large Hadron Collider (LHC) that will start operation in 2007, heavy ion physics faces a new era where not only the available energy is extended by another order of magnitude but also the importance of this field of physics is underlined when for the first time an accelerator is created providing the highest available energy for heavy ion and particle physics at the same time.

Current Theoretical Understanding of Heavy Ion Collisions

Provided that the beam energy is sufficient to reach the phase transition, a relativistic heavy ion collision is expected to proceed in the following way: The fireball produced in the collision goes through a short pre-equilibrium phase where the partons from the collided nuclei interact and new partons are produced. It then quickly reaches the QGP phase, where thermal equilibrium prevails. By expanding, the fireball then cools down, until the critical conditions for a phase transition back to hadronic matter are fulfilled. At this point of *chemical freezeout*, inelastic interaction stops and thus the particle abundances remain unchanged from here on. Upon further expansion, the point of *thermal freezeout* is reached where elastic interactions cease. This determines the shape of particle spectra.

Lattice QCD predicts the critical energy density that has to be overcome for reaching the QGP phase to be at $\epsilon_{\mathrm{C}} \approx 1$ GeV/fm^3, or the tenfold of normal nuclear density. It can be achieved by heating normal nuclear matter or raising the baryonic chemical potential μ_{B} through compression. Figure 2.1 shows the phase diagram of strongly interacting matter. The position of the phase transition line depicted is determined by lattice QCD. The critical endpoint E [4] marks the change from a first order phase transition at higher μ_{B} to a cross-over transition below. The chemical freezeout parameters for heavy ion collisions are included as points, the lines depict trajectories along which the

[1] An explanation of kinematical terms used is given in Appendix B

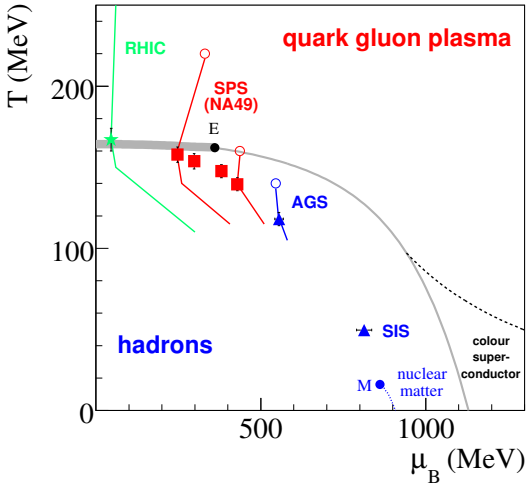

Figure 2.1: Phase diagram of strongly interacting matter. Points indicate the chemical freezeout conditions for heavy ion collisions at various energies. The lines describe the adiabatic expansion of these systems from thermalisation to thermal freezeout.

systems produced in the collisions evolve from thermalisation up to thermal freezeout. For RHIC energies as well as the top SPS energy of $\sqrt{s_{\mathrm{NN}}} = 17.3$ GeV, the phase border is well crossed, and there is strong evidence that it is first touched at the lower SPS energies.

Signatures of the Quark-Gluon Plasma

Different observables that would point out a QGP formation were suggested and tested in experiments [5]. None of them alone could doubtlessly prove the creation of a new state of matter. The latest stage of the SPS heavy ion programme [6] therefore consisted of nine experiments partly specialised on certain observables. Their common announcement [3] about "a new state of matter" discovered was thus based on a complete picture achieved by considering these different signatures together. These signatures found in the observed strangeness production, flow or fluctuations or stemming from the interpretation of interferometry results are mostly based on the high particle abundances produced in processes with low momentum transfer, i.e. *soft* processes.

Signatures indicating the production of a QGP at RHIC in addition include a multitude of observables stemming from processes with high momentum transfer, called *hard*

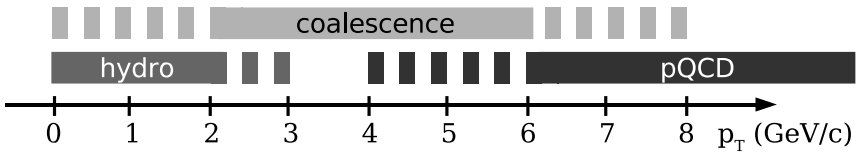

Figure 2.2: A rough sketch of the models that describe hadron production in different ranges of p_{T}.

processes. When at the very early stage of the collisions partons from the incident nuclei interact with very high momentum transfer, the scattered partons emerge at large angles with respect to the original beam direction. This is manifested in the high transverse momentum (p_{T}) of the jets of hadrons evolving from these partons. While pQCD can describe the jets in elementary reactions, the environment affects them in A+A collisions. A *jet quenching* is seen in the suppression of inclusive particle production at high p_{T} in central nucleus-nucleus reactions. The suppression gets weaker when the size of the surrounding nuclear medium decreases and is therefore interpreted as radiative energy loss of partons in a dense colour charged medium.

A given p_{T} spectrum of partons produced in primary hard collisions can transform into the resulting hadron spectrum in different ways. Two hadronisation mechanisms are competing: the *fragmentation* of one parton into hadrons and the *recombination* or *coalescence* of multiple partons to form one hadron. An example: The formation of a meson with $p_{\mathrm{T}} = 3$ GeV/c via coalescence needs two quarks of $p_{\mathrm{T}} = 1.5$ GeV/c, while in the fragmentation picture a parton with $p_{\mathrm{T}} > 3$ GeV/c would be required. The latter process may be more effective, but as the parton spectra quickly decrease with p_{T}, it may play a minor role because the low p_{T} partons are more abundant. A smooth transition of hadronisation mechanisms is expected as the origin of hadrons throughout their p_{T} spectrum. While in the low p_{T} region soft processes are dominant that lead to hadron abundances that can be described in hydrodynamical models, coalescence might play a role at intermediate p_{T} roughly between 2 and 4 GeV/c. Currently, different implementations of coalescence models [7] consider the coalescence between soft partons only or also include coalescence between soft and hard partons. Fragmentation of partons from hard processes gains prevalence at higher p_{T}. A very rough sketch showing the possible origin of hadrons at different p_{T} is given in Fig. 2.2.

The quark coalescence picture has been experimentally supported when it was realised that the anisotropic flow measured at RHIC follows a valence quark scaling at intermediate p_{T}. Another hint to particle production through quark coalescence is an

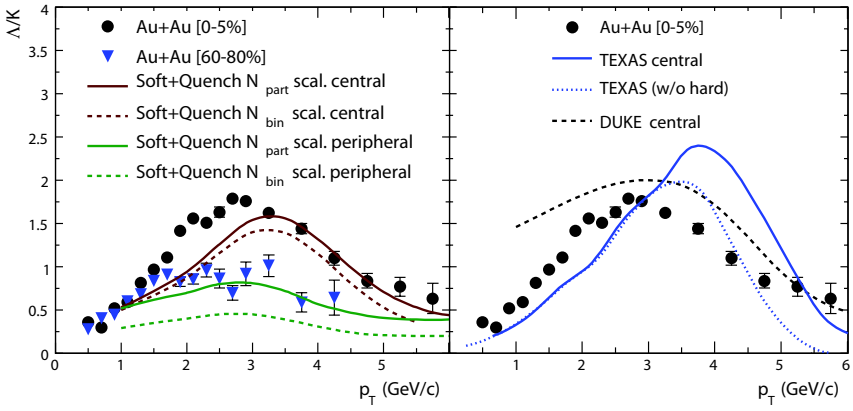

Figure 2.3: The $\Lambda/\mathrm{K}^0_\mathrm{S}$ ratio as a function of p_T for central and peripheral Au+Au collisions at $\sqrt{s_\mathrm{NN}} = 200$ GeV, compared to coalescence models. The figure is taken from [8].

enhancement of baryon over meson production in this p_T region. Measurements find baryon / meson ratios to fail expectations from hydrodynamical models but to be higher than pQCD predictions in the p_T region of 2 GeV/c $\leq p_\mathrm{T} \leq$ 4 GeV/c. A very recent result on these effects can be found in [8]. Figure 2.3 is taken from this publication. It shows the $\Lambda/\mathrm{K}^0_\mathrm{S}$ ratio measured in Au+Au collisions at $\sqrt{s_\mathrm{NN}} = 200$ GeV in the STAR experiment, and a comparison to various coalescence models.

The reach in p_T is lower at SPS energies than at RHIC. Nevertheless, the region up to $p_\mathrm{T} \approx 4$ GeV/c is accessible at the top SPS energy (see e.g. [9]). The NA49 experiment is capable of detecting and identifying hadrons in a wide range of p_T. Within the NA49 collaboration analysis is proceeding on the high p_T production of charged hadrons and of neutral strange hadrons. The common results have been presented in [10]. This thesis describes the analysis process for the neutral strange hadrons K^0_S and Λ.

Chapter 3

The NA49 Experiment

Today, the NA49 collaboration consists of 94 physicists from 23 different institutes. Since the idea for this experiment came up, many hundreds have participated in the design, development and construction of the detector, the electronics and the software that all are necessary to make the physics processes under investigation accessible to analysis. And beyond that, members of the collaboration have spent beam times from 1994 to 2002 taking the data. This and the following chapter give an overview of this work that is the indispensable basis for the analysis presented in this thesis.

The name NA49 derives from the experiment's location in the North Area, one of CERN's experimental sites. It is a fixed target experiment served by the H2 beam line of the *Super Proton Synchroton* (SPS). Section 3.1 briefly describes the accelerators used and Section 3.2 gives an overview of the NA49 setup. A more detailed description of the detector can be found in [11]. In Section 3.3, emphasis is placed on the main tracking detectors of NA49, the TPCs. The electronics involved in the data taking and recording are presented in Section 3.4 and the modifications for the data sample on which this analysis is based are discussed.

3.1 Particle Accelerators at CERN

The CERN accelerator complex consists of a wide variety of accelerators to provide lepton, hadron and ion beams for the various experiments in the fields of particle and heavy ion physics. Figure 3.1 shows a schematic plan of the accelerators. To reach the experiments of the heavy ion programme, Pb ions coming from the ion source pass a

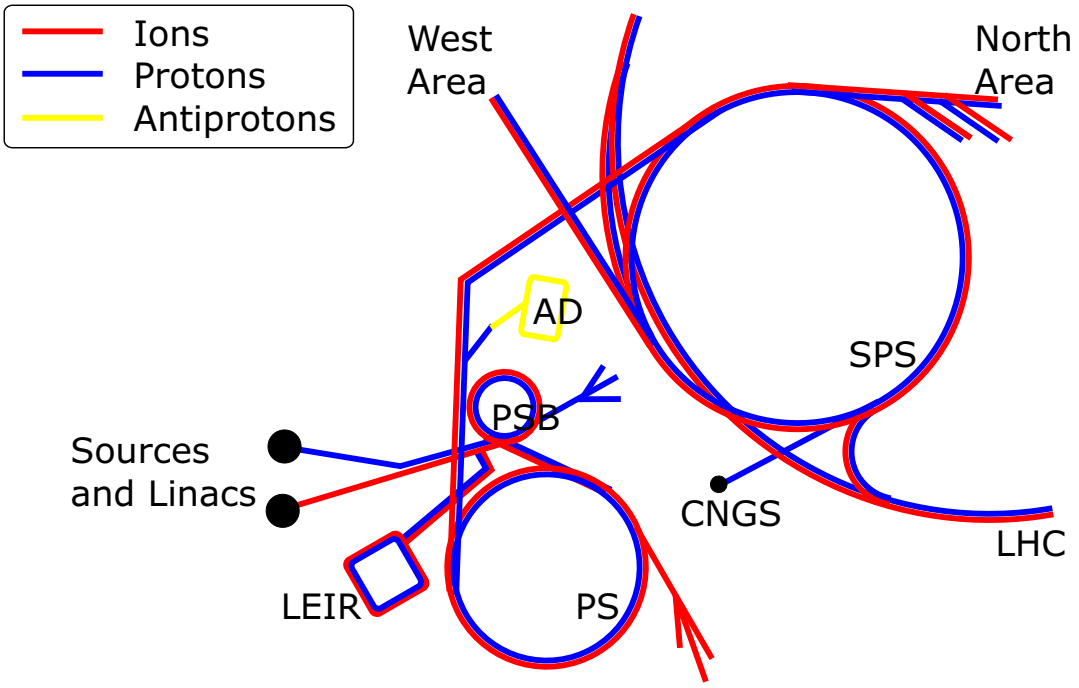

Figure 3.1: Parts of the CERN accelerator complex. Shown are the Antiproton Decelerator (AD), PS Booster (PSB), Proton Synchrotron (PS), Low Energy Ion Ring (LEIR), Super Proton Synchrotron (SPS) and parts of the Large Hadron Collider (LHC). The experimental facilities shown are the SPS North and West areas as well as the CERN Neutrinos to Gran Sasso (CNGS) production facility.

chain of accelerators with increasing output energy: the linear accelerator LINAC3, the PS Booster (PSB), the Proton Synchroton (PS) and finally the SPS. The accelerators are linked together and can provide different beams to various experiments at the same time. Their operation is therefore organised in so called *supercycles*, the combination of acceleration *cycles* for different purposes. For the PS, a typical supercycle at the time of data taking of the heavy ion experiments took 19.2 s and contained four ion fillings for the SPS of 1.2 s each. In the remaining time, needed by the SPS for the acceleration, the PS can serve other purposes, e.g. providing p beams to experiments or conducting accelerator tests in "machine development" cycles. The SPS cycle also took 19.2 s, the beam was extracted over a time period of 4.2 s and split up into six beam lines [12].

Since its foundation in 1954, CERN played an important role in accelerator development [13]. When the PS came into operation in 1959 [14], its 24 GeV proton beam took over the world record for the highest energy available from the Synchrophasotron at the Joint Institute for Nuclear Research (JINR) in Dubna, Russia. The beam intensity rose since then by a factor of about 10^3, also through the addition of the PS Booster syn-

chrotron in 1972. Completed in 1976, the SPS was CERN's first accelerator exceeding its main site near Meyrin, Switzerland. The underground accelerator ring has a diameter of 6.9 km. The experimental halls for fixed-target experiments are situated in the West Area (WA) on the main site and the North Area (NA) near Prevessin, France. In addition, the SPS features two underground experimental areas, where $p + \overline{p}$ collisions were studied in collider mode from 1981 until 1990. Protons can be accelerated in the SPS to a maximum energy of 450 GeV, for ions it is limited to 400 GeV per charge unit.

The chain of accelerators used by the heavy ion programme was originally built to provide proton or electron beams for high-energy physics experiments. The production of ion beams started in 1986 with the acceleration of ^{16}O, followed by ^{32}S shortly after that. These isotopes were eventually brought to a beam energy of 200A GeV in the SPS. This beam was used by the first generation of SPS heavy ion experiments. Following the installation of the new Electron Cyclotron Resonance (ECR) ion source and a new linear accelerator (LINAC3) [12], ^{208}Pb ions at 158A GeV were available from 1994 on. This is equivalent to a total energy of $\approx$ 33 TeV per Pb ion. The newer generation of SPS heavy ion experiments recorded data until 2004. Besides the top energy Pb ions, the H2 beam line can provide smaller nuclei (e.g. Si, C) from a fragmentation target or protons, all at various energies. This made the SPS size and energy scan programme (see Section 2.2) possible.

Following CERN's principle to reuse existing infrastructure, PS and SPS were used to pre-accelerate electrons and positrons for the Large Electron Positron Collider (LEP). And also when the Large Hadron Collider (LHC) enters into operation, PS and SPS will provide the proton (from 2007 on) and Pb ion (2008) beams to be further accelerated in the LHC. Future fixed target experimental activity at CERN [15] may include an extended system size and energy scan programme of a new collaboration using an upgraded version of the NA49 detector to search for the critical point of the QCD phase diagram [16],[17]. Another proposal is the NA60 collaboration's request to take further data on Pb+Pb collisions [18].

3.2 Detector Concept

The NA49 detector [11] is a large acceptance spectrometer, designed to track and identify the charged hadrons produced in nucleus-nucleus (A+A), proton-nucleus (p+A) and proton-proton (p+p) collisions. Considering the high charge of the ion beam as well

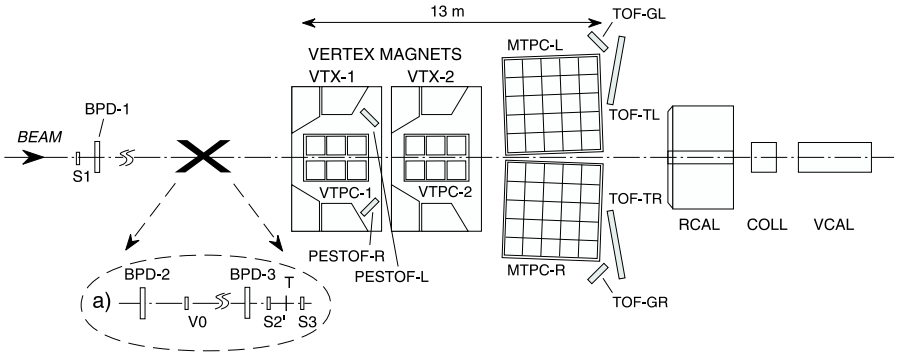

Figure 3.2: Schematic setup of the NA49 experiment. The figure is taken from [11].

as the high number of particles produced in A+A interactions, the detector design had to be geared to the requirements for these collisions. The high beam charge requires a low material budget in the passage of the beam. The high multiplicity calls for good resolution tracking detectors combined with strong magnetic fields. For this purpose, Time Projection Chambers (TPCs) as main tracking detectors were the natural choice. The resulting schematic layout is shown in Figure 3.2. This section describes the setup as it was used for recording central Pb+Pb collisions at 158A GeV in 1996. Changes specific for the dataset used in the presented analysis are explained in Section 3.4.

In the most central Pb+Pb interactions at the top SPS energy of 158A GeV, approximately 1,700 charged hadrons are produced (in contrast to about 10 in p+p reactions). To separate this large number of particle tracks, downstream of the target two superconducting dipole magnets expand the cone of produced particles. Together, they can provide a maximum bending power of 9 Tm. The aperture inside the yoke has a constant height of 1 m and a horizontal width increasing in downstream direction, giving room for tracking detectors.

Four large volume TPCs[1] serve as tracking detectors, the two Vertex TPCs (VTPC1 and VTPC2) lie within the magnetic field while the Main TPCs MTPC-L and MTPC-R are situated downstream of the magnets. The particles' momenta are determined by tracking their paths through the magnetic field. Depending on the phase space region, a momentum resolution between $\mathrm{d}p/p^2 = 3{\cdot}10^{-5}(\mathrm{GeV}/c)^{-1}$ and $\mathrm{d}p/p^2 = 7{\cdot}10^{-4}(\mathrm{GeV}/c)^{-1}$ is reached. In addition to tracking, the TPCs provide a measurement of energy loss per unit of length ($\mathrm{d}E/\mathrm{d}x$) in the detector gas. As the energy loss is a function of the particle

[1] The basic principles on TPCs are described in Section 3.3

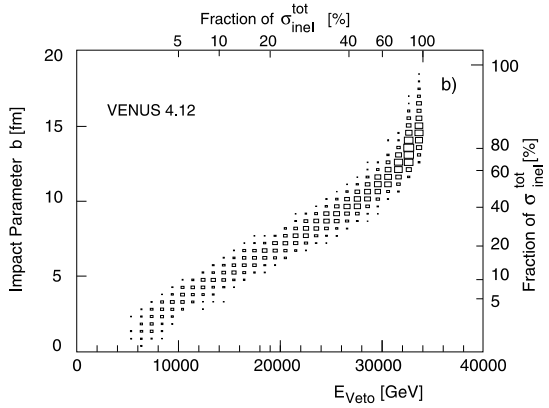

Figure 3.3: Mapping of E_{Veto} (energy measured in the VCAL) to collision parameters calculated with the VENUS model. The figure is taken from [11].

velocity,[2] particle identification can be obtained through simultaneous measurement of momentum and $\mathrm{d}E/\mathrm{d}x$. So, $\mathrm{e}^{\pm}$, $\pi^{\pm}$, $\mathrm{K}^{\pm}$, p, $\overline{\mathrm{p}}$, d and $\bar{\mathrm{d}}$ can be distinguished in the momentum region where the Bethe-Bloch curve is in *relativistic rise*. The geometrical acceptance of the TPCs is limited by the fact that the region around the beam axis is excluded from its sensitive volume. The Pb beam particles would deposit too much charge in the detector. Nevertheless, 70% of all charged particles are accepted.

The particle identification capability of the TPCs is complemented through velocity measurements in the phase space region, where the specific energy loss functions of different particles overlaps. This has been implemented in the Time Of Flight (TOF) detectors consisting of finely granulated scintillator walls.

Also for the beam counters the aim was to minimise the amount of material in the beam. For this reason, the beam counters for the A+A setting of NA49 were chosen to be a thin (200μm) Quartz Cherenkov detector (S1) and two thin He gas Cherenkov detectors (S2' and S3). The beam counters measure the beam charge, so S1 and S2' are used to select incoming Pb ions. In the case of an inelastic interaction in the target, the signal in S3 is lower hence an anticoincidence of the beam counters upstream of the target with it is used as a trigger signal. S1 furthermore starts the TOF measurement. The three Beam Position Detectors (BPD) consist of proportional chambers. By extrapolating from the hits in the BPDs to the target position, the main interaction vertex can be determined with an accuracy of 40μm.

[2]The energy loss of charged particles in the passage of matter is described by the Bethe-Bloch equation. Particle identification through $\mathrm{d}E/\mathrm{d}x$ measurement only plays a minor role in this analysis and has been described in detail before, e.g. in [19]

The centrality of the A+A collisions is determined by a measurement of projectile spectators in the Veto Calorimeter (VCAL). Therefore, the collimator COLL has an aperture allowing neutrons, protons and fragment nuclei with beam momentum to reach the calorimeter. A low energy deposit then refers to a central collision and vice versa (see Figure 3.3).

To start a measurement, *trigger detectors* send a signal to the detector control when several conditions are fulfilled. The beam counters and the VCAL serve as trigger detectors. To select a central Pb+Pb collision, a Pb ion has to be recognised in the beam counters before the target S1 and S2'. At the same time, S3 behind the target has to measure a lower value than the two, indicating a target interaction. To add centrality selection, this is combined with the requirement of an energy measurement below a threshold in the Veto calorimeter.

All coordinates given in this thesis refer to the NA49 coordinate system: The z-axis follows the beam direction, y represents the drift direction of electrons in the TPCs (upwards) and x (pointing towards the jura mountains) completes them to a right-handed system. The origin lies in the centre of VTPC2, the target (depending on the run period) at $z \approx -580$ cm.

3.3 The Time Projection Chambers

TPCs are detectors capable of recording the tracks of charged particles in three dimensions. They consist of proportional chambers for the two-dimensional readout, extended by a large gas volume. This gas volume is surrounded by a field cage providing a homogeneous electric field, the *drift field*, which allows the determination of the third coordinate.

The NA49 TPCs have a cuboidal shape, the drift field is applied between the base plate and the readout chamber on the top end, so it is antiparallel to the y-axis in all four TPCs. Strips of Mylar foil coated with aluminium define the field on the sides with a minimum amount of material to be traversed by the particles. By this a homogeneous field of 200 V/cm (VTPC) and 170 V/cm (MTPC), respectively, can be provided over the large volume of the TPC. On its way through the detector gas, a charged particle ionises gas molecules. The drift field accelerates the electrons towards the readout chamber. A constant drift velocity results from an equilibrium between the acceleration and the

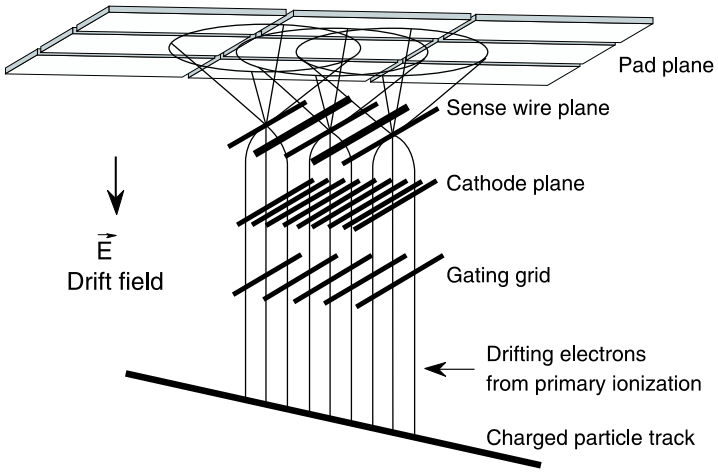

Figure 3.4: Layout of the TPC readout chamber. The figure is taken from [11].

energy loss through elastic interaction with the gas molecules. This proportionality between drift time and space in drift direction permits the determination of the y-coordinate.

In the readout chambers, the drifting electron clouds are converted into electronic signals from which their three dimensional position as well as their total charge (which is proportional to the energy initially deposited by the ionising particle) can be reconstructed. The readout chamber consists of three wire planes and a readout plane segmented into pads (see Figure 3.4). Electrons produced by an ionising track will first encounter the *gating grid*. In case of a trigger signal, the voltage corresponding to an undisturbed drift field is applied, making the gating grid permeable for electrons. Without a trigger, alternating wires are brought to ± 100 V relative to the drift field, preventing electrons from entering the readout chamber. The gating grid also hinders ions produced in the gas amplification from moving into the drift volume where their space charge would cause problems. The *cathode plane* is at 0 V potential and separates the drift field from the amplification field of the proportional chamber. The *sense wire plane* alternately consists of sense wires, which possess a potential of ≈ 1 kV, and of field wires at 0 V. Gas amplification takes place in the vicinity of the high potential sense wires, where the electric field is not homogeneous but proportional to r^{-2} with respect to the wire centre. An avalanche of electrons is produced, multiplying one electron to $2 \cdot 10^4$ in the VTPCs and to $0.5 \cdot 10^4$ in the MTPCs. The electrons are quickly absorbed by the wires, leaving the heavier thus slowly drifting ions behind. Their space charge induces a mirror charge on the readout pads. The current building up this mirror

charge is amplified on the Front-End Cards (FEC), sitting directly on the back of the readout plane. One FEC processes the signals from 32 pads by amplifying, shaping and digitising them. The total drift length of the chambers (VTPC: 0.66m, MTPC: 1.1m) is equivalent to a drift time of 50μs. 512 time samples are extracted at 10MHz in the normal configuration. For high statistics-runs, only 256 time bins at half the sampling rate were recorded (see Section 3.4). Control and Transfer (CT) boards collect the signal from 24 FECs and send them to the counting house via optical fibres. The further way of the signals is described in Section 3.4.

The segmentation of the readout plane into pads follows the track geometry. Having a rectangular shape, the pads have lengths of $16-40$ mm but widths of only $3.5-5.5$ mm, as a higher resolution is required perpendicular to the tracks to be able to separate two tracks lying close to each other. For the same reason, the alignment angle of the pads is adapted to the most common track direction. A sequence of pads perpendicular to the tracks is referred to as a *pad row*. The space resolution of the TPC is better than the pad dimensions, as the simultaneous measurement of one charge cluster on neighbouring pads is used to calculate the charge distribution's centre of gravity during the reconstruction (see Section 4.2). The same is done in y direction over several time bins.

3.4 Data Flow

Receiver boards located in the counting house pick up the signals from four CT boards each. Their function is to reduce the raw data size and to buffer the information until it is required by the *event builder*, a CPU arranging the raw data of all detectors. The event building is necessary because the transfer from the detector is done unsorted to increase speed. From the event builder, the raw events are transferred to a tape recorder.

Of all "three-dimensional pixels" made up by one pad $\times$ one time bin, only a fraction contains charge from a track. A considerable amount of memory can be economised when the empty bins are not saved. The residual signal for all pads is therefore recorded with no beam present and then substracted from the measured signal. Points with a signal below a threshold of 5 ADC counts are not stored. This reduces the raw event volume by 90%. During the $\approx$ 5 s of one SPS spill, in average 30 central Pb+Pb events are selected by the triggers. A maximum of 32 events can be buffered on the receiver boards. While data transfer from the detector to the receiver boards is in progress, the buffered information is not accessible for the event builder. During the spill, only few events can

be transferred to the event builder to free the buffer position occupied by them. This means that the buffer limits the maximum event rate and that the largest part of event building is done in the $\approx$ 15 s between two spills. The events are then recorded by a Sony DIR-100M tape recorder at a writing speed of 16 Mbyte/s. An equivalent of 12,000 central Pb+Pb events fits on one of the Sony D1 cassettes with a capacity of 100 Gbyte each.

2000 High Statistics Run

Between 1994 and 2002, the NA49 collaboration has collected a wide variety of data. Table 3.1 lists the nucleus-nucleus collisions studied in the system size and energy scans. In addition, a large set of hadron-hadron and hadron-nucleus interactions has been recorded for reference. For the 158A GeV Pb beam run in 2000, several changes were done to the setup described above. The aim was to attain a high statistics sample of central Pb+Pb collisions to be able to look for very rare observables. Analyses conducted with this data set span from the search for a ϕ signal in the $\phi \rightarrow e^+e^-$ decay channel [20] to the study of Λ flow [21] and Ω and $\overline{\Omega}$ production [22]. It also plays an important role in ongoing analyses on various topics. This section describes the changes done to achieve the higher event rate needed here. They are summarised in Table 3.2 on page 25.

Only counting the TPCs, an amount of $182,016$ individual channels has to be read out. As the ADCs operate with a precision of 8 bit, at standard time sampling rate this leads to $182,016 \cdot 512 \cdot 8\text{bit} \approx 90\text{Mbyte}$ of raw data flow to the receiver boards per event. Although data compression on the receiver boards reduces the size to 8 Mbyte, their buffer can only hold 32 events. A reduction of the raw event size by 50% was achieved by halving the time sampling rate in the analog to digital conversion from 512 to 256 time bins. The smaller events can then be transferred more quickly to the event builder, leaving buffer slots for reuse in the same spill.

With the detector ready to process more events, the following measures could be taken to increase the interaction and the trigger rates:

- The target thickness was changed. In the 1996 setup, the Pb foil had a density thickness of 224 mg/cm^2, for the 2000 run period, it was replaced by one with 336 mg/cm^2. The thicker target provides a higher interaction probability, but a potential problem arising from it is the equally higher probability of γ conversions

System	Beam energy	Centrality	No. of events
Pb+Pb	158A GeV	10%	800k
		23.5%	3M
		minimum bias	410k
	80A GeV	7%	300k
	40A GeV	7%	700k
		minimum bias	430k
	30A GeV	7%	440k
		35%	230k
	20A GeV	7%	360k
		35%	330k
Si+Si	158A GeV	12%	300k
	40A GeV	29%	130k
C+C	158A GeV	15%	220k
	40A GeV	66%	240k

Table 3.1: Datasets on nucleus-nucleus collisions recorded with the NA49 experiment.

in the target.

- The beam intensity was increased. For the 2000 runperiod, it was on average 30% higher than in 1996, making double events more probable. They are excluded by an online monitor rejecting events if a second beam particle is within a short time window after a collision. But it also happens more frequently that beam particles traverse the detector without causing another target interaction while an event is recorded. On their way through the detector gas, the Pb ions can produce δ-electrons in electromagnetic interactions with the gas molecules. Having low momenta around 100MeV, these electrons leave long spiral tracks in the VTPCs, influencing the track recognition. This problem is treated in detail in Section 5.7.

- Finally, the centrality selection was modified to accept more events. The Veto calorimeter energy threshold for the trigger was raised to accept less central collisions as well.

These steps could raise the event rate to 40 per spill (from an average of 30 in the

1996 run) enabling NA49 to record nearly 3 million events in the three weeks of data taking.

	1996 run period	2000 run period
Time bins	512	256
Target density thickness	224 mg/cm^2	336 mg/cm^2
Interaction probability	0.5%	0.75%
Beam particles per spill	$\approx 80,000$	$\approx 100,000$
Centrality selection	10%	23.5%
Recorded events per spill	≈ 30	≈ 40

Table 3.2: Setup changes for the 2000 high statistics data taking period.

Chapter 4

Data Processing in NA49

Just as important as the actual detector setup is the computer hardware and software enabling physicists to examine the collected data and to extract the information that is needed to interpret the processes observed. On the hardware side, NA49 relies on clusters of computers and large data storage facilities situated at CERN. They are presented in Section 4.1. The software consists of three major parts: The reconstruction chain (Section 4.2) finds tracks in the raw ADC counts and stores momentum, energy loss and other information about the particles observed in so-called Data Summary Tape (DST) files. To further investigate this information, the object-oriented analysis-framework ROOT (Section 4.3) provides the necessary tools. The third important part of software is the simulation environment that is essential in interpreting the measurements. It is described in Section 4.2.

4.1 Hardware Resources at CERN

Data Mass Storage

The raw data collected over NA49's nine years of running adds to a total of 100 Tbyte. To access this raw data for processing, a second Sony DIR-100M tape drive was installed in a tape robot holding up to 24 tapes, or 2.4 Tbyte at the same time. As data on tape is not randomly accessible, every tape system needs to be complemented by disk pools where the data is temporarily staged when in use. For the Sony robot, a stage pool with a capacity of 900 Gbyte was used. The raw data has been reconstructed and is now

accessible in the DST files. The Sony system is thus no longer needed and was phased out in the end of 2005. But parts of the raw data are still required: Samples from every run period have to be retained for embedding (see Section 4.4), and some datasets will be reprocessed to include more information into the DSTs. For this purpose, 7.5 Tbyte have been copied from the Sony tapes to the *CERN Advanced STORage Manager* (CASTOR) prior to the phase-out.

While the Sony system has been installed by the NA49 collaboration and was only used within the experiment, CASTOR is a CERN-wide installation, maintained and operated by the CERN IT division [23],[24] currently holding a data volume of 4.4 Pbyte. The project is in the process of preparing for the even larger data streams that will be recorded by the LHC experiments. CASTOR, being in operation since 2001, is a storage manager enabling access to the data kept on tape from a large number of different operating systems. It is a hierarchical storage manager, because the files contained are accessed via path names with organisation in directories like in a standard unix file system, so that the user does not need to know on which tape a particular file is stored. So one internal part of CASTOR is the name server mapping these path names to the actual file location on tape, other components are handling and controlling the transfer from tape to stage pools. The most important module visible to the user is the `rfio` package providing command line facilities to create, access or remove files on CASTOR and an API enabling the communication between applications and CASTOR.

Computing Clusters

To avoid long distance transfers of data, processing and analysis of the data stored in CASTOR are done on computing farms that are also located at CERN. PLUS (Public Login User Service) provides a cluster of computers for interactive logon, *lxplus*. It is operating under Scientific Linux CERN 3 (SLC3). All CERN users can use it to develop and test software, access the Mail and News Servers, their AFS (Andrew File System, [25]) home directory and many other services provided by the CERN IT Division. The data stored on CASTOR can also be accessed via lxplus.

A batch farm consisting of $\approx$ 1,500 computers (*lxbatch*) is provided for more time-consuming and CPU-intensive processes. They are likewise running under SLC3. The software LSF (Load Sharing Facility) takes care of the distribution of batch jobs to the computers in the farm and for allocation of computing power to the different experiments. NA49 has a share of on average 100 jobs running in parallel on lxbatch.

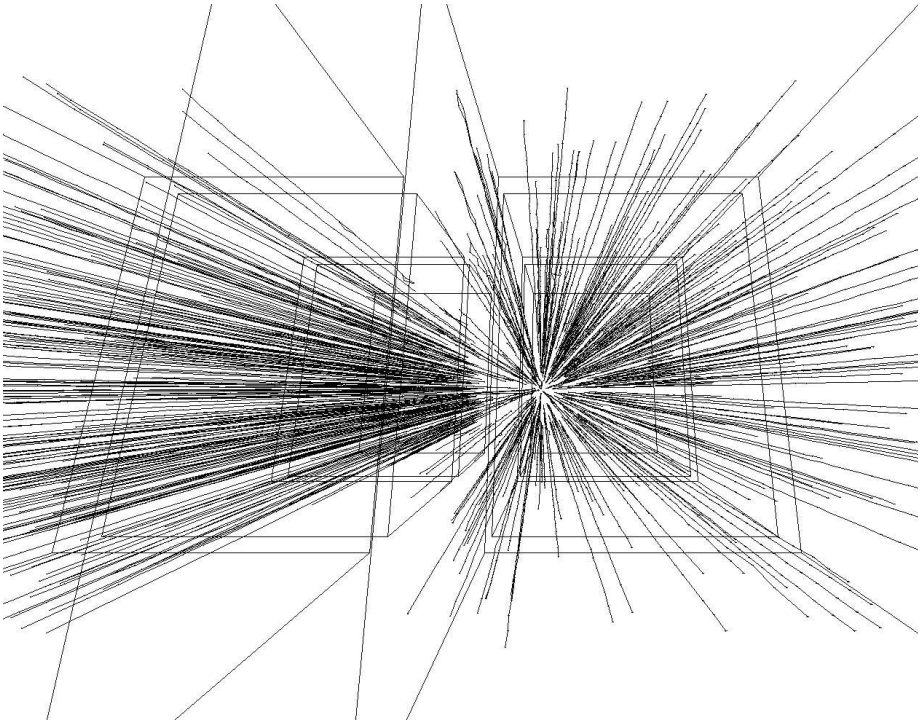

Figure 4.1: Reconstructed tracks in VTPC2.

4.2 Reconstruction Chain

The reconstruction chain's role is to convert the raw data into DST files for making the physics information gathered in the experiment accessible to analysis. While this was traditionally done in a single-threaded process, a different approach was used in NA49: DSPACK [26], a client/server architecture developed for this purpose. The reconstruction procedure is split into many client processes. This structure was supposed to make distributed development and debugging easier. The small size clients are better than single-thread solutions in terms of performance and ressource usage. Other advantages are that client software can be written in different programming languages, that the clients can be reused in different steps of the reconstruction, and that clients can easily be exchanged or modified. DSPACK files like the DSTs used in NA49 can be directly accessed; for other files like the raw data format plug-ins are required. A DSPACK server connects all the pieces by providing the communication between input and output files and the clients.

The reconstruction of each event starts with the merging of pixels from the raw data into space points. Corrections have to be applied on the points to determine the

real positions where a track has traversed the detector. The next step is to assemble the corrected points for forming tracks and later for joining tracks that may originate from secondary vertices like those of V^0 decays. These are the most essential parts of the reconstruction for the analysis presented in this thesis. They and the clients involved are described in more detail below. The sequence of the reconstruction process is schematically depicted in Fig. 4.2 on page 31.

Many other clients complete the reconstruction by gaining information from hits in the TOF detectors, calculating the $\mathrm{d}E/\mathrm{d}x$ etc.

Cluster Finding and Corrections

The `dipt` client does the cluster finding in all TPCs. On the plane spanned by a pad row and the drift time in raw data coordinates, neighbouring pixels containing charge are combined to form a charge cluster. The position of its centre of gravity is converted to the NA49 coordinate system. The true position of the charge underlies several distortions. The drift in the VTPCs does not exactly follow the electric field due to $\vec{E} \times \vec{B}$ effects in the regions where the magnetic field is not parallel to the electric field. This is taken care of by the `vt_ncalc` client. Distortions due to inhomogeneities in the electric field are settled in the `edisto` client. Variations in the signal propagation delay between the different channels are corrected by `tpc_calib`.

With the resulting points, a first attempt is made to assemble tracks. A phenomenological correction table is calculated from the remaining systematic position deviations between corrected points and reconstructed tracks [27]. Before the actual tracking, these corrections are applied in the client `tpc_res_corb`.

Tracking

The environment to form tracks from the space points is different for each TPC. The VTPCs exhibit very high track densities, making it hard to discriminate tracks. But the magnetic field that is present here allows for momentum determination independent of the track's origin. In the MTPCs, tracks are easier to separate. But a particle's momentum can only be calculated with the assumption that the track originates from the main interaction vertex. To make use of the advantages complementing each other, a global tracking scheme has been developed [28]. It subsequently runs local tracking

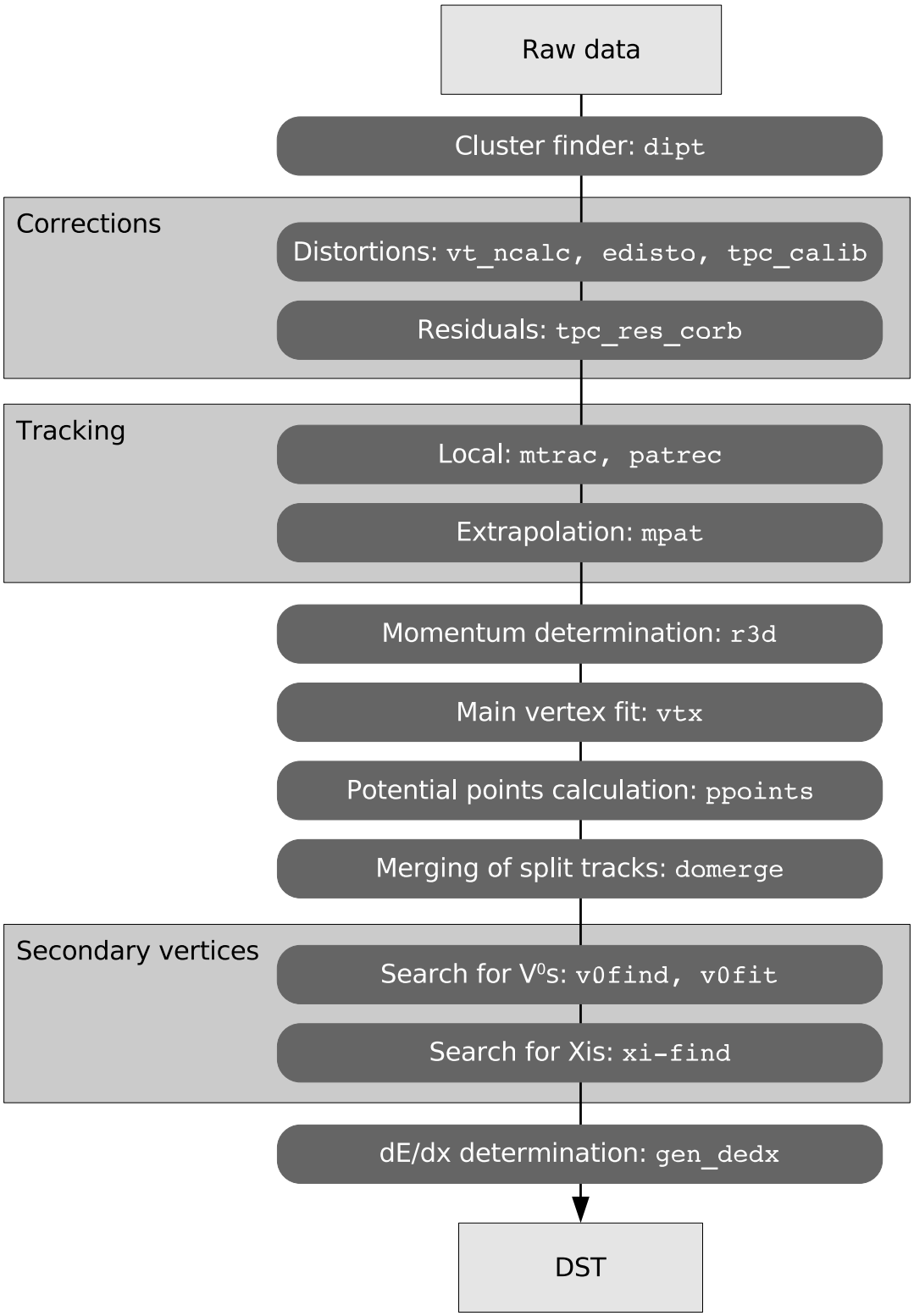

Figure 4.2: Flow chart for the reconstruction chain. The steps of the reconstruction process are depicted together with the involved clients.

clients to find track parts in a single detector and then connects it to points measured in other TPCs. In the beginning, those tracks that can be easily identified are looked for. The points associated to tracks that have already been found are removed, so the point density decreases. This makes the recognition of more complicated track geometries feasible in the later stages. `mtrac`, the client for the MTPCs, uses straight lines as a track model, while `patrec` for the VTPCs has to describe the particle tracks in the magnetic field by a helical trajectory. The third client involved in the global tracking scheme is `mpat`, doing the extrapolation to other TPCs. Thereby "extrapolation" means calculating the trajectory according to the known magnetic field and attaching measured points to the track that are found close enough to the prediction.

The process starts with `mtrac` at the downstream end of the MTPCs, where the track density is the lowest. The tracks found there are extrapolated to VTPC2. The points belonging to those MTPC tracks that do not find matching points in VTPC2 are released to be reused later. On the remaining points in VTPC2, `patrec` performs local tracking and the tracks found thereby are extrapolated to the MTPCs. All tracks are now extrapolated to VTPC1. MTPC tracks, for which points in VTPC1 suggested by the extrapolation are not found, are discarded and their points released. Local tracking on the remaining VTPC1 points is done, and the tracks found are extrapolated to the MTPCs.

To save the information obtained in the tracking, the DSTs provide two different data structures: `rtrack` and `track`. The first stands for raw track and holds all information about a particle that is independent of assumptions. The position of the particle's first and last point or the number of points left in the detectors is stored here along with the momentum at the first measured point that has been calculated by the momentum reconstruction client `r3d` based on the track curvature in the magnetic field. After this first momentum fit, the client `vtx` determines the main vertex position by a fit on the closest approach of all tracks.

This fitted main vertex position is included as the origin of the track, when the momentum is calculated for a second time to be stored in the `track` structure. So, a `track` contains the information about a particle valid under the assumption about its origin. From the `track`, there is always a link to the `rtrack` it is based on. When searching for secondary vertices later on, it is possible to find more `track`s to the same `rtrack`. It is then left to the later analysis to clarify whether a particle comes from the main vertex or a secondary vertex.

For each track, the *impact parameters* b_x and b_y are determined. They denote the difference in x and y between the fitted main vertex position and the track's extrapolation back to the target z position. Furthermore, the *number of potential points* is calculated by counting how many pad rows were traversed by the reconstructed track. This is the number of points on the track that would have been recorded under ideal circumstances. For the V^0 analysis it is important to mention that the potential points are calculated for the assumption that each particle comes from the main vertex. It may thus not be correct for secondary particles. These values are also stored in the `rtrack` structure.

The tracking is completed by clients that add particle identification information to the tracks like the energy loss measured in the TPCs [19] or the time of flight measured in the TOF detectors [29]. Other clients make sure that the track of one particle has not been identified as two separate tracks [30]. As the analysis presented in this thesis mainly builds up on the reconstruction of the secondary V^0-vertices as described below, I will not go into more detail here.

Reconstruction of V^0 particles

In NA49, K^0_S, Λ and $\overline{\Lambda}$ can be identified via their V^0 decay topology (see Section 1.2). These decay channels going into two oppositely charged particles are listed in Table 4.1 together with their most important properties. The other possible decay modes have neutral daughter particles and are thus not visible to the detectors. To find the decay products of V^0 particles in the high number of reconstructed tracks, the `v0find` client combines pairs of oppositely charged tracks and retains them as candidates, if certain *cut criteria* are fulfilled. In the course of V^0 analyses in NA49, two different approaches have emerged. They are named after the institutes where they were developed: While the *Birmingham* method [31] possesses different cuts depending on where the daughter tracks are found, the *GSI* procedure [32] features one set of cuts for all detector regions. The latter has proven to be less susceptible to inhomogeneities in the efficiency and has successfully been applied in the Λ analysis [33]. Also in the presented analysis, the GSI cut criteria were used. They are explained below, and their numerical values are summarised in Table 4.2. For all candidates remaining after the cuts, the `v0fit` client refits the momentum of the potential V^0 particle and the position of the decay vertex .

A first cut on single tracks makes sure that the momentum of a potential daughter particle can be determined without assuming the main vertex as origin. Therefore only

Particle	Quark content	Decay channel	Branching ratio	Q
K^0_S	$1/\sqrt{2}\,(s\bar{d} + d\bar{s})$	$\rightarrow \pi^+\,\pi^-$	68.95%	0.219 GeV/c^2
Λ	u d s	$\rightarrow$ p π^-	63.90%	0,038 GeV/c^2
$\overline{\Lambda}$	$\bar{u}\,\bar{d}\,\bar{s}$	$\rightarrow \bar{p}\,\pi^+$	63.90%	0,038 GeV/c^2

Table 4.1: V^0 particles and their decay channels [34].

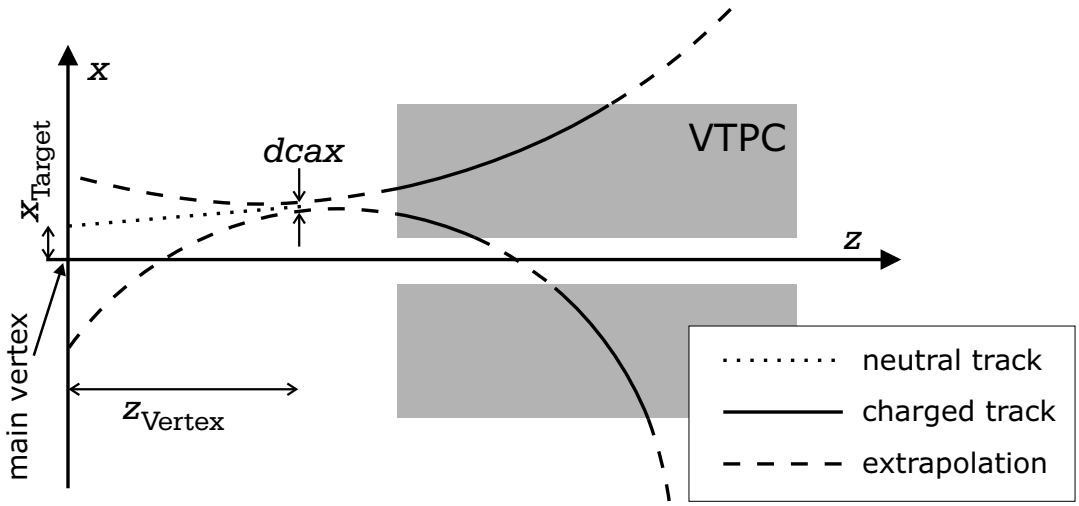

Figure 4.3: Schematic explanation of the variables used in the V^0 finder (xz-plane).

tracks exceeding a *minimum number of points* in the VTPCs are considered.

Now, geometrical cuts are applied to the pairs that may potentially form a V^0 vertex. They are illustrated in Figures 4.3 and 4.4. To apply these cuts, the accepted tracks are extrapolated towards the target, and their *distance of closest approach* (DCA) is determined in x and y direction. Thus, *dcax* and *dcay* must be below a threshold to pass this cut. Background in form of combinations of primary tracks that may appear like V^0s is concentrated close to the target. Hence, the DCA is only considered at z-values larger than the z_{Vertex} cut variable. For a further reduction of this background source, the *dip*-cut requires that the track projections to the yz-plane cross at z-values larger than z_{Dip}. Here, a linear extrapolation is sufficient, as the yz-plane is perpendicular to the bending plane.

The extrapolations of the potential daughter tracks are required to have a certain *separation* at the target plane. In the Birmingham V^0 finder cuts, this was applied in

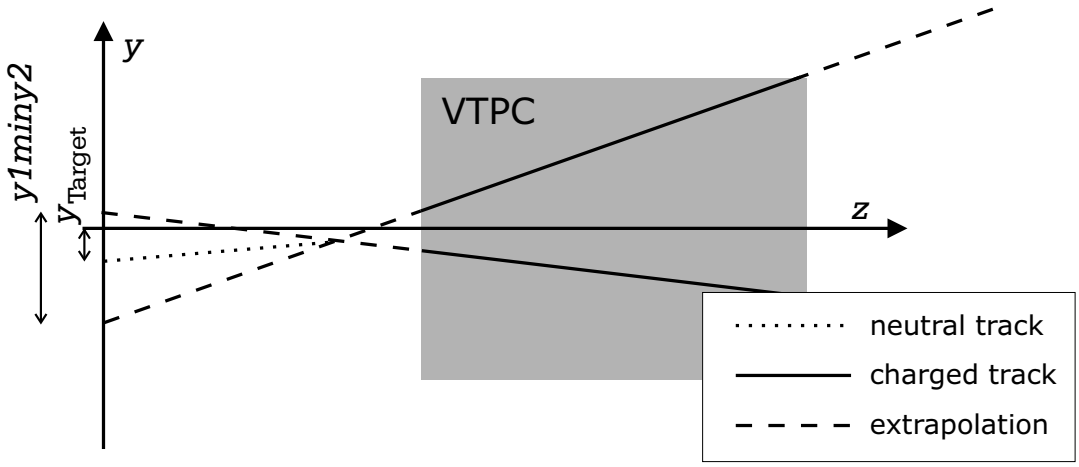

Figure 4.4: Schematic explanation of the variables used in the V^0 finder (yz-plane).

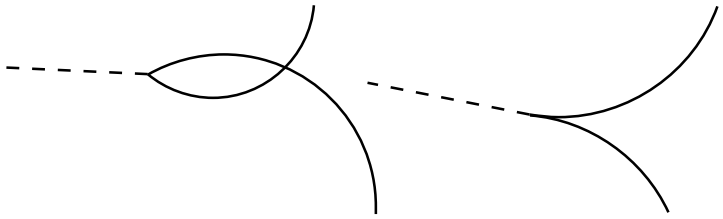

Figure 4.5: Two different V^0 decay topologies: The "Cowboy" (left) and the "Sailor" (right).

the x direction; in the GSI set, it is replaced by a cut on the y separation $|y1miny2|$. The original $|x1minx2|$ cut turned out to reject valid tracks with high transverse momentum [32]. Simply cutting out all main vertex tracks by their impact parameter would also reject many true V^0 daughter particles.

Figure 4.5 shows the difference between two V^0 decay topologies: The "Cowboy" and the "Sailor". For the former, the crossing may be mistaken for the decay vertex when the decay plane defined by the daughter particles' momenta coincides with the bending plane. To prevent false reconstructions, a cut is applied on the angle ϕ. It is defined as the angle between the normal to the decay plane, and the vector that is perpendicular to the V^0 particle's momentum $\vec{p}_{\mathrm{V}}$ and lying in the plane spanned by $\vec{p}_{\mathrm{V}}$ and the y-axis.

Now the x and y coordinates of the assumed V^0 particle at the target plane (i.e. their *impact parameters*) are extrapolated. The cut is rather loose, as later in the reconstruction V^0s that do not stem from the main vertex are used in the multi-strange

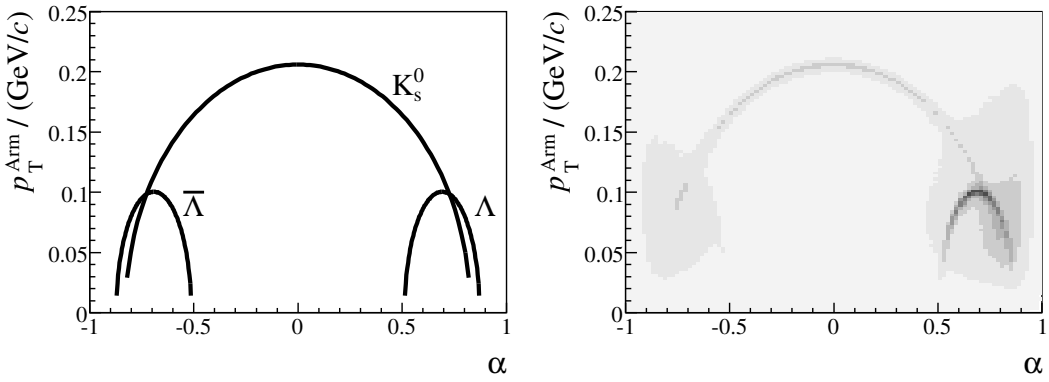

Figure 4.6: The Armenteros-Podolanski plot in idealised form (left) and as measured (right).

hyperon reconstruction. While here, the absolute values of the x and y coordinates are considered, later in the analysis (see Chapter 5) the difference to the main vertex position determined by the BPDs is used instead for a more precise treatment of the impact parameters.

The only kinematical criterion used in the V^0 finder is the cut on the *Armenteros transverse momentum* $p_{\mathrm{T}}^{\mathrm{Arm}}$. It is defined as the absolute value of one daughter particle's momentum component transverse to the original V^0 direction of motion. Due to momentum conservation, it is the same for both daughter particles. From their momentum components longitudinal to the direction of the V^0 momentum, one can derive the quantity

$$\alpha = \frac{p_{\mathrm{L}}^{+} - p_{\mathrm{L}}^{-}}{p_{\mathrm{L}}^{+} + p_{\mathrm{L}}^{-}} \tag{4.1}$$

where p_{L}^{+} (p_{L}^{-}) is the positive (negative) daughter's momentum component along the V^0 momentum. Together, α and $p_{\mathrm{T}}^{\mathrm{Arm}}$ span the *Armenteros-Podolanski plot* as shown in Figure 4.6. Possible decays of each V^0 species form half ellipses in this diagram. Their centres lie on the α-axis, at a value defined by the daughter particle's mass difference. For the symmetric decay $\mathrm{K}_{\mathrm{S}}^0 \to \pi^+\pi^-$, it is the origin. For $\Lambda \to \mathrm{p}\pi^-$ it is positive, as the heavier proton always carries a larger momentum than the pion. For $\overline{\Lambda} \to \overline{\mathrm{p}}\pi^+$, the opposite case is valid. The reach in $p_{\mathrm{T}}^{\mathrm{Arm}}$ is determined by the decay's Q value. Where the lines cross, the different particle species cannot be distinguished.

The `v0fit` client does a nine-parameter fit to find the three coordinates each of the

Cut	value
Required points in	
VTPC1	$N_{\text{Points}} \geq 10$
VTPC2	$N_{\text{Points}} \geq 20$
Distance of closest approach in	
x	$dcax \leq 0.50$cm
y	$dcay \leq 0.25$cm
z-position of decay vertex	$z_{\text{Vertex}} \geq -555.0$cm
Tracks must cross in yz-plane behind	$z_{\text{Dip}} = z_{\text{Vertex}} - 5.0$cm
Separation of daughter particles at target in	
x	no cut
y	$\lvert y1miny2\rvert \geq 0.75$cm
Angle of V to bending plane	$0.2 \leq \phi \leq 2.9$
Impact parameter of V^0 particle in	
x	$\lvert x_{\text{Target}}\rvert \leq 25.0$cm
y	$\lvert y_{\text{Target}}\rvert \leq 25.0$cm
Armenteros p_{T}	$p_{\text{T}}^{\text{Arm}} \leq 0.35$GeV/c

Table 4.2: V^0 cuts applied by the `v0find` client in the reconstruction.

V^0 decay vertex and the daughter particle momenta. It also calculates the *invariant mass* under the three possible assumptions about the daughter particles' identities. The invariant mass method is dealt with in detail in Section 5.3. Appendix B explains how it is calculated. The V^0 candidate is saved to the DST in a `vertex` structure with links to the daughter particles as new `tracks`.

4.3 The Analysis Framework ROOT

ROOT [35],[36] is an object-oriented analysis framework developed in the context of NA49 for the needs of analyses in the fields of heavy ion and high energy physics. On the advent of the LHC experiments and the challenges expected from the analysis of their huge amounts of data, procedure-oriented data analysis software like PAW (Physics Analysis Workstation) were at their limits. Their successor ROOT, implemented in C++, is not only mature enough to deal with the LHC data, but is even used in other

fields today. ROOT is available on many platforms.

As a framework, ROOT provides the basic ressources a user often needs. These are classes for histograms with their filling, analysis and display methods, mathematical functions with the ability to e.g. do fits to measured distributions and input/output facilities for accessing and storing the data analysed. Among the collection classes in ROOT the data container *tree* is an important tool to organise the data. Along with ROOT comes the C++ interpreter CINT. C++ basically is a compiled language, but CINT manages to execute scripts at a speed of up to 60% of the compiled version. It can be used both as a command line and as a script interpreter for development, testing or just to generally run shorter programs.

ROOT Mini-DSTs

The evolution of the size of an event in NA49 starts with ≈ 90 Mbyte raw data coming from the detector, and is reduced to 8 Mbyte at the time of recording (see Section 3.4). After reconstruction, in the DSPACK DSTs each event still needs 2–3 Mbyte which is not so easily manageable when analysing many events. Therefore the DSTs are converted to *ROOT mini-DSTs*, which only contain the most relevant information, but on the other hand only need 150-200 kbyte per event. In each mini-DST, the information is arranged as a ROOT tree, making it easily accessible during analysis.

All produced mini-DSTs together make up a data volume of 1.35 Tbyte. They are stored in CASTOR like the DSTs, but are kept permanently staged in a special pool, making sure that they are always accessible for analysis without the delay caused by recalling from tape.

ROOT49

ROOT was extended to *ROOT49* [37] through the addition of the *T49* classes specific to NA49. The T49 classes are subdivided into

- Mini-DST Classes (T49DST) for the storage of the information extracted from the DSTs in the mini-DST tree. Examples are `T49ParticleRoot` for holding the most important data from the DSPACK `track` structure (see Section 4.2), or `T49VertexRoot` for storing the information about vertices e.g. V^0s.

- Analysis Classes (T49ANA) providing tools for the mini-DST analysis like applying cuts or analysing $\mathrm{d}E/\mathrm{d}x$ information.
- DSPACK Interface Classes (TRootDS) allow the access to DSPACK DSTs and can be used when copying the information from them to mini-DSTs.

The abilities of ROOT49 in connection with the small size of the mini-DSTs are the prerequisite to analyse a large number of events in a reasonable time. The 3 M events used in this analysis require $\approx$ 500 Gbyte space and can be analysed within a day on the lxbatch cluster (see Section 4.1).

4.4 Simulation Chain

The measurement of particle spectra in the NA49 experiment underlies some constraints: The geometrical acceptance is limited and the reconstruction chain has inefficiencies in finding tracks or decay vertices in the high track density environment of heavy ion collisions. Also through quality cuts applied in the analysis (see Section 5.2), parts of the signal may be lost. To correct for these effects, a simulation chain is installed, recreating the detector in the computer. It can simulate the detector response to any experimental situation, which is then processed through the normal reconstruction chain. At the end, input and reconstruction results are compared in the *matching* process, allowing to determine the influence of *geometrical acceptance*, *reconstruction inefficiency* and *cut inefficiency*. Two approaches can be followed: The simulation result can either be analysed as is or, to study the realistic influence of the track density, it can be superimposed on a real event (*embedding*). The simulation chain is outlined in Fig. 4.7 on page 40.

GEANT

GEANT (GEometry ANd Tracking) [38] is a software package developed at CERN to allow simulation studies of high energy physics experiments. The principal components are the *detector geometry description package* and the *tracking* that simulates the passage of particles through matter. Today, GEANT is used in many fields of science, not only for detector simulation, but also in medical research or in space science to evaluate the effect of radiation on spacecraft. While the most recent version is GEANT4, NA49's

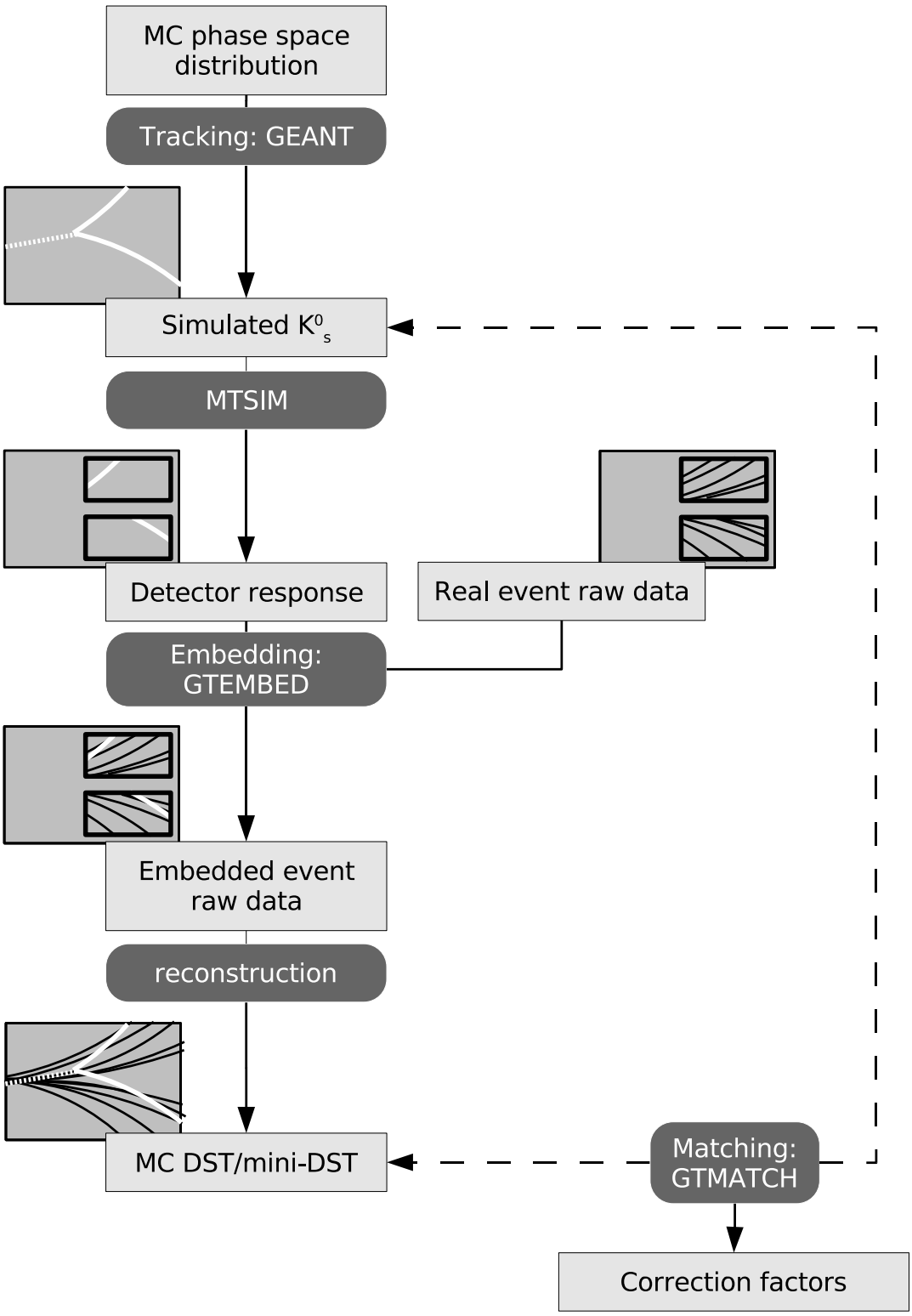

Figure 4.7: Flow chart for the simulation chain.

implementation under the name *GNA49* is based on GEANT3. As an input, GEANT requires the momenta of the particles to be simulated. These come from Monte Carlo (MC) event generators like VENUS, or from simple random distributions from known spectra.

In the detector geometry description, each piece of material used in the detector construction is reproduced in the computer: support structures and detector material like the TPC gas. Magnetic field distributions are also needed as input.

In the tracking, all relevant physics processes are simulated that can occur to the different kinds of particles at the passage of a detector: decays, bremsstrahlung, Compton scattering, hadronic interactions, $e^+ + e^-$ pair production, particle-antiparticle annihilation, multiple scattering and many more. Ionisation of the detector gas is also implemented and by this clouds of electrons orginate in the simulated TPCs. These *idealised space-points* are converted to the DSPACK format by G2DS.

MTSIM

In the NA49 simulation chain, the program MTSIM turns the idealised space-points into the electronic signals that would have been produced by the readout electronics of the experiment. Real measured raw data underlies certain distortions that are corrected in the reconstruction process (see Section 4.2). To be able to process the simulated raw data with the same chain, the inverse of these corrections is applied before. The clients that apply the corrections are also capable of doing the inverse. The output of MTSIM is raw data in the DSPACK format that can either be directly analysed or embedded into the raw data of a real event.

Evaluation of the Simulation results

Embedding is done in the `gt_embed` client. The raw data from the simulation and from the real event are added for each pad $\times$ timebin point. Saturation in the readout electronics occurs when the charge registered by one channel exceeds a certain value. This is also taken into account here. The resulting raw data file can then be reconstructed via the normal reconstruction chain (see Section 4.2), which is only altered to make sure that the original simulated information is also stored with the results as it is needed for the next step.

To determine the acceptance and efficiency, a procedure evaluates which simulated particles have been reconstructed. This is denoted *matching* and done in the `gtmatch` client. It starts with the *point matching*, where for each GEANT generated space point corresponding reconstructed points in proximity are searched for. In each plane spanned by a pad row and the drift direction, the distance is evaluated both in y direction and perpendicular to it. Two points match if they lie within a rectangle of $0.5 \times 0.5\text{cm}^2$. This criterion is loose enough that the matching also works in areas of the detector where distortions prevail. The point matching may be ambiguous. This is reduced in the *track matching*, where multiple points along a track have to fit together. A reconstructed track is accepted as a match to a simulated track, when a minimum of 5 of its measured points in a VTPC (or 10 in a MTPC) match to the according simulated points. For a simulated V^0 particle, the condition is even stricter, as both daughter tracks have to match. Nevertheless, the result is still not unique, and it has to be clarified in the later analysis which is the best match. This can be achieved by comparing the number of matched points or other measures for the different matches (see Section 5.4).

The result of the simulation chain is a DSPACK DST, which in addition to the reconstruction results contains the information about the simulated particles with links to the reconstructed tracks that were identified as matches. This is also reflected in the special MC mini-DSTs to which the output is copied for further analysis.

More detailed information about the simulation chain developed in NA49 can be found in [39] and [40].

Chapter 5

V^0 Analysis up to High p_T

With the fundamental methods that have been described in the preceding chapters, it is possible to analyse the production of neutral strange particles up to a reach in p_T that is only limited by their abundance dropping quickly with p_T. This chapter sumarises the steps required to conduct such an analysis.

The events that were used are presented in Section 5.1 together with the criteria for their choice. On the basis of the V^0 candidates found during reconstruction (see Section 4.2), criteria are now refined to provide the prerequisite for a reliable statistical particle identification for K^0_S and Λ in any region of phase space. The other essential parts of the analysis, signal extraction and corrections for acceptance and efficiency are discussed in Sections 5.3 and 5.4, respectively. The cut criteria (presented in Section 5.2) are optimised for the requirements in the high p_T region and the results checked for consistency (see Sections 5.5 and 5.6).

5.1 Dataset and Event Cuts

Acceptance is not a limiting factor for the V^0 analysis up to high p_T in NA49. But as particle yields drop exponentially with growing p_T, high statistics is a prerequisite for this analysis. Therefore, the central Pb+Pb dataset recorded in 2000, with a total of 3 M events, was chosen. The changes in the experimental setup for this data taking are described in Section 3.4. The trigger was set to accept the 23.5% most central of the total inelastic cross section. Following calculations in the VENUS model [41], this corresponds to a number of wounded nucleons of $\langle N_W \rangle = 267$.

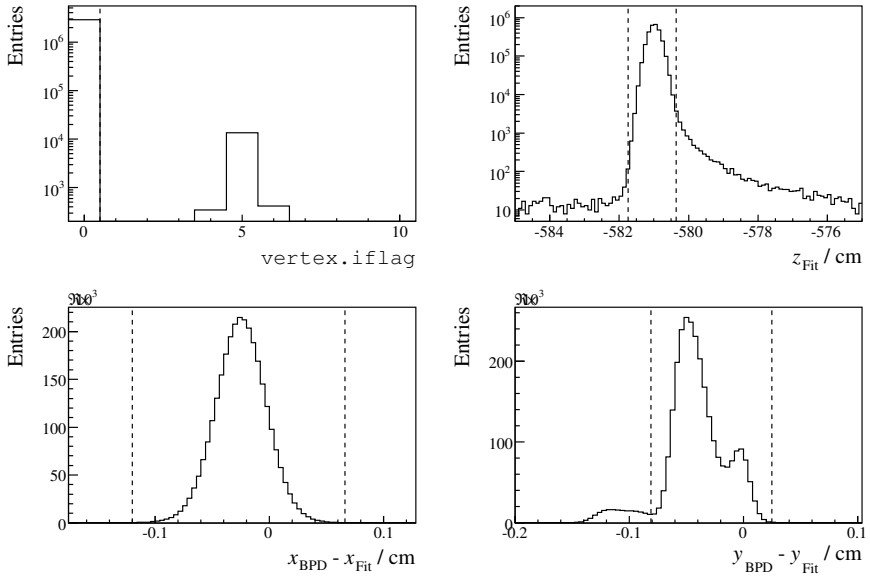

Figure 5.1: The event properties used in event cuts for the studied dataset. Dashed lines indicate the values of the event cuts.

To ensure that the selected event sample does not contain events from non-target interactions or other error sources, *event cuts* are applied. The first quantity that is considered is a flag that has been set to each event during the reconstruction (see Section 4.2). If the fit on all tracks to determine the main vertex position converges after some iterations, the `vertex.iflag` is set to 0. In case that the fit diverges or other problems occur during the reconstruction, it is set to non-zero values. Only events with `vertex.iflag` $= 0$ are analysed here. Another criterion to judge the quality of an event is the accord between the fitted vertex position and the position obtained in the independent BPD measurement. For the z coordinate, the real target position is known to be at $z = -581.0$ cm. A symmetrical cut around this value on the fitted z-position rejects possible non-target interactions. In x and y, the difference between fitted and measured position is considered in the cut. Too large differences indicate a failed main vertex fit and are therefore excluded. All quantities used for the cuts are shown in Fig. 5.1. The cut values and the effects of the individual cuts as well as the total impact of the cuts are summarised in Table 5.1. The largest fraction of rejected events comes from the $y_{\mathrm{BPD}} - y_{\mathrm{Fit}}$ cut. The other cuts only have a minor influence.

The total number of available events is 2,911,405. After cuts, 2,692,133 remain for the analysis.

Cut	Effect
`vertex.iflag` $= 0$	0.49%
$-581.74\mathrm{cm} < z_{\mathrm{Fit}} < -580.36\mathrm{cm}$	0.55%
$-0.120\mathrm{cm} < x_{\mathrm{BPD}} - x_{\mathrm{Fit}} < 0.066\mathrm{cm}$	0.11%
$-0.081\mathrm{cm} < y_{\mathrm{BPD}} - y_{\mathrm{Fit}} < 0.025\mathrm{cm}$	6.62%
Total	7.53%

Table 5.1: The event cuts and the fraction of events failing the cut if applied separately.

5.2 Analysis Cuts

The cuts applied in the V^0 finder (see Section 4.2) have been chosen in such a way that as few real particles as possible are rejected. Another constraint is to also retain non-primary V^0s from multi-strange hyperon decays. The cuts are thus very loose and lead to *combinatorial background* in the invariant mass spectra. The background consists of combinations of primary charged tracks or wrong combinations with secondary particles that pass the criteria of the V^0 finder. A high background makes the signal extraction (see Section 5.3) more difficult and increases the statistical error on the yield. The cuts are refined in the analysis to reduce background and improve the signal to background ratio. Too strict cuts on the other hand remove real particles from the list of V^0 candidates which is not acceptable when looking for rare probes like the high p_{T} particles.

For the analysis presented in this thesis, different sets of cuts have been compared and their effects studied. While the values of the cuts are discussed in Sections 5.5 and 5.6, the quantities on which these cuts are applied are explained in the following. They are divided into cuts on the properties of a potential decay vertex (V^0 *Cuts*) on one hand, and into *track cuts* on the individual daughter tracks on the other hand. After the cuts have been exerted, there may be ambiguities in the attribution of daughter particles to V^0 vertex candidates. These are resolved by the *cleaning procedure* described at the end of this section.

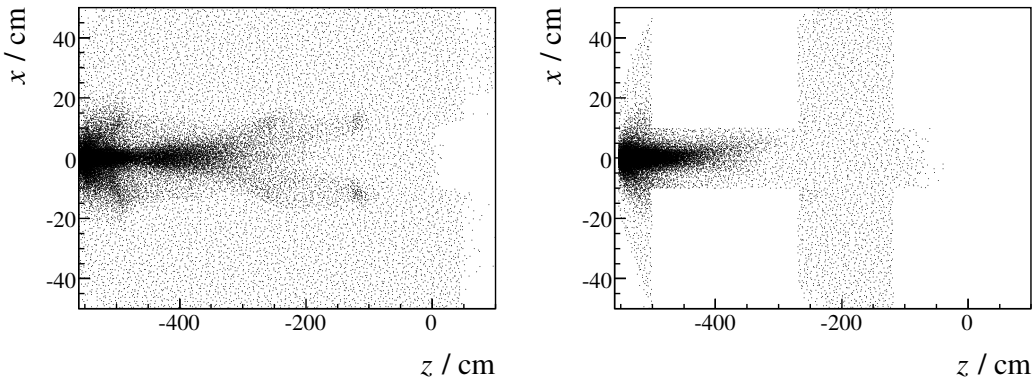

Figure 5.2: The decay vertex positions of the V^0 candidates before (left) and after the cuts (right). The effect of the z_{Vertex} cut can be seen at small z values, the excluded boxes are the sensitive TPC volumes.

V^0 Cuts

Decay Vertex Position

Already during the reconstruction (see Section 4.2), a cut on the z position of the decay vertex is applied. The closer to the target the V^0 vertex is, the more the background from combinations of primary tracks plays a role. But also valid candidates with a short lifetime have low values of z_{Vertex}. In this analysis, the influence of a stricter cut on this has been studied.

A source of reconstruction inefficiency is given by decays that take place inside the sensitive volume of a TPC. Their emerging daughter tracks may overlap and may be difficult to discern. Only V^0 candidates with a decay vertex outside of the sensitive volume are therefore accepted. The distribution of the positions of the V^0 candidates is shown in Fig. 5.2

Impact Parameters

After the Xi-finder has used all V^0 candidates during the reconstruction of multi-strange hyperons (see Section 4.2), candidates for secondary V^0 particles are not required in the list of primary V^0s any more. They remain in the DSTs, but when copying to mini-DSTs, cuts on the impact parameters are applied to save storage space and to reduce

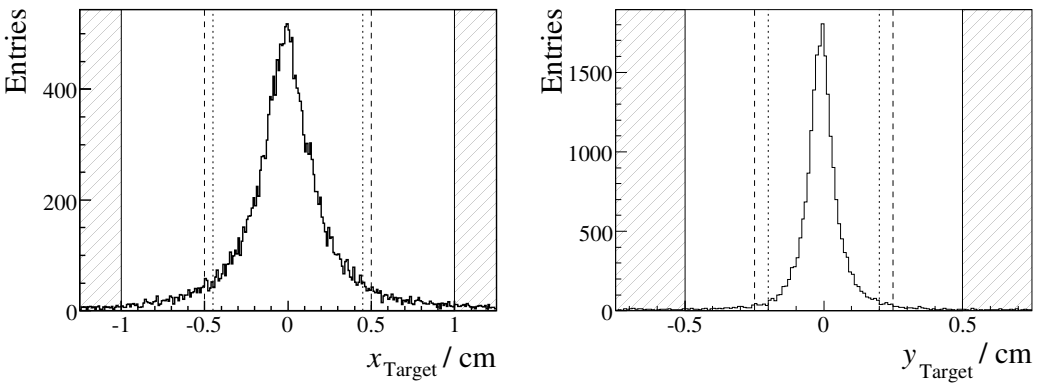

Figure 5.3: The resolution in x_{Target} and y_{Target} as determined in the simulation. The hatched area shows values excluded when copying to mini-DST, while lines indicate the different cuts applied in the analysis.

combinatorial background. With the values

$$|x_{\text{Target}}| \leq 1.0 \text{ cm and } |y_{\text{Target}}| \leq 0.5 \text{ cm},$$

these cuts are stricter than what has been applied in the V^0 finder. Yet still the resolution in x_{Target} and y_{Target} is so good, that $\approx 85\%$ of the true V^0 particles lie within the criteria used. The resolution shown in Fig. 5.3 has been determined in the simulation (see Section 5.4). The background can significantly be lowered by a cut on the impact parameters. During the analysis, different values for this cut have been compared. As mentioned before (see Section 4.2), the real distances in x and y to the main interaction vertex are used now instead of the positions at the target plane which were sufficient for the looser cuts applied during reconstruction.

Decay Angle - $\cos\Theta^*$

The decay of a V^0 particle is isotropic in its own rest frame. This means that the number of daughter particles emitted per solid angle element $\mathrm{d}\Omega^*$ is the same for each angle, $\mathrm{d}N/\mathrm{d}\Omega^* = \text{const}$. The decomposition of the solid angle into a polar and an azimuthal component Θ^* and ϕ^*, with respect to the mother particle's momentum in the laboratory rest frame is expressed by $\mathrm{d}\Omega^* = \sin\Theta^*\mathrm{d}\Theta^*\mathrm{d}\phi^*$. This leads to

$$\frac{\mathrm{d}N}{\mathrm{d}\left(\cos\Theta^*\right)} = \text{const.}$$

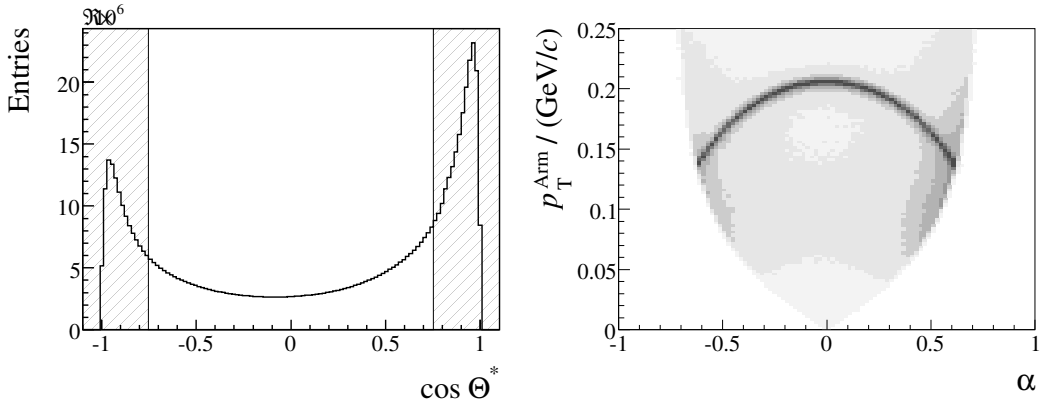

Figure 5.4: The $\cos\Theta^*$ distribution of all reconstructed V^0 candidates (left). The effect of a cut excluding the hatched area can be seen in the Armenteros-Podolanski plot (right).

The distribution of true V^0 particles in $\cos\Theta^*$ is thus flat, while the background is not uniformly distributed in this variable (see Fig. 5.4). A cut on $\cos\Theta^*$ can help to reduce the background, but any cut on it removes parts of the signal as well.

Track Cuts

Track Quality

The quality of a primary charged track can, amongst other possibilities, be determined by considering the ratio of measured to potential points. By requesting this to be larger than 50%, split tracks, i.e. tracks that are reconstructed as two tracks, can be excluded. The number of measured points (N_{Points}) and the number of potential points ($N_{\text{PotPoints}}$) are determined during reconstruction (see Section 4.2). For secondary charged tracks there may be a drawback in using the potential points. Their calculation during the reconstruction is based on the primary track assumption, so it may not be correct for the true V^0 particles. Such a cut on the point ratio would remove too much of the signal.

A different approach to judge the quality of the daughter tracks is the total number of measured points. As every cut must be reproducible in the simulation, the point distribution from measured data and simulation has been compared. To get a clean sample of data, the background was suppressed by other cuts. Additionally, a phase space region was chosen, where practically no background is present with the given cuts. The comparison between measurement and simulation is shown in Fig. 5.5. Both agree

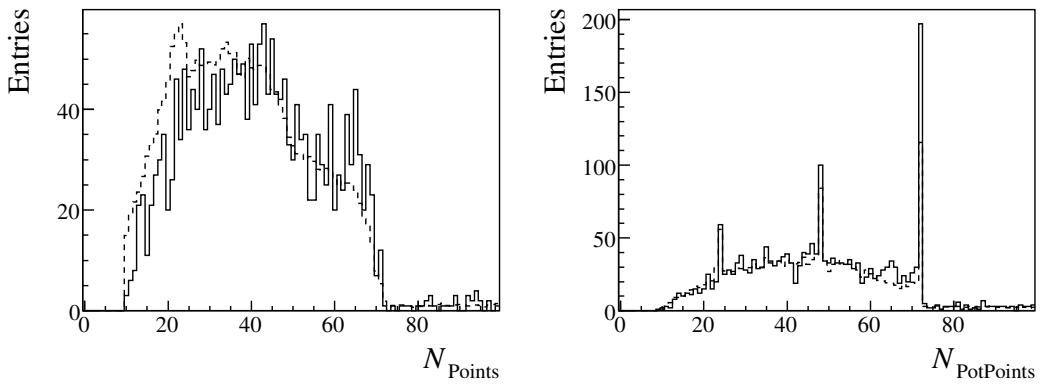

Figure 5.5: The N_{Points} and $N_{\text{PotPoints}}$ distributions for the positive daughter tracks of the reconstructed V^0 candidates (dashed histogram lines) as well as from simulated particles (solid lines). Only the interval $1.41 < y < 2.41$, $0.6\text{GeV}/c < p_T < 2.0\text{GeV}/c$ was used where the cut CO (see Section 5.5) provides a practically background-free sample.

quite well, but N_{Points} was chosen to be used for cuts.

Momentum of the Daughter Particles

Earlier analyses ([32],[33]) showed that the reconstruction efficiency drops for V^0 particles with low momentum daughter tracks. This is explained by the pad geometry in the VTPCs being optimised for primary charged tracks. Secondary particles with a low momentum have large deviations from the optimal trajectory. To avoid this inefficiency, a cut accepting only daughter particles with a momentum above a certain value is suggested.

Cleaning Procedure

One `rtrack` can be assigned during the reconstruction to more than one V^0 candidates. Even after cuts, this ambiguity remains to some extent (see Fig. 5.7). As only one of the V^0 candidates can be a real particle, the others have to be rejected to avoid multiple counting of particles. To reveal the best candidate, their impact parameters are compared, and the one with the lowest is chosen to remain. The impact parameter as a criterion for the best V^0 candidate has been chosen arbitrarily. As the differences between the impact parameters of the multiple candidates is not very large and the

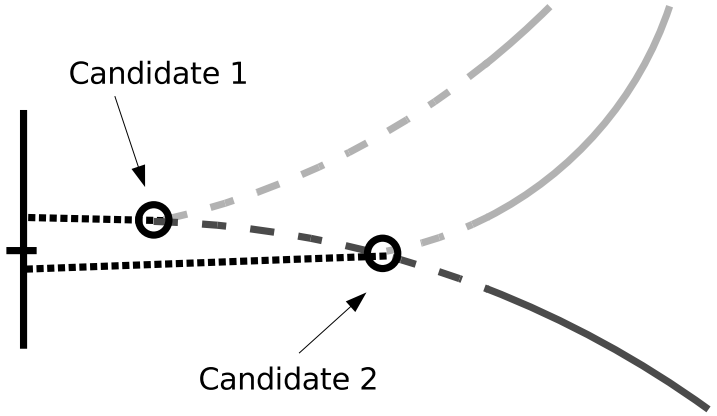

Figure 5.6: The "cleaning" procedure: The dark grey track appears as the daughter track of two V^0 candidates. Only one of them can be a real particle.

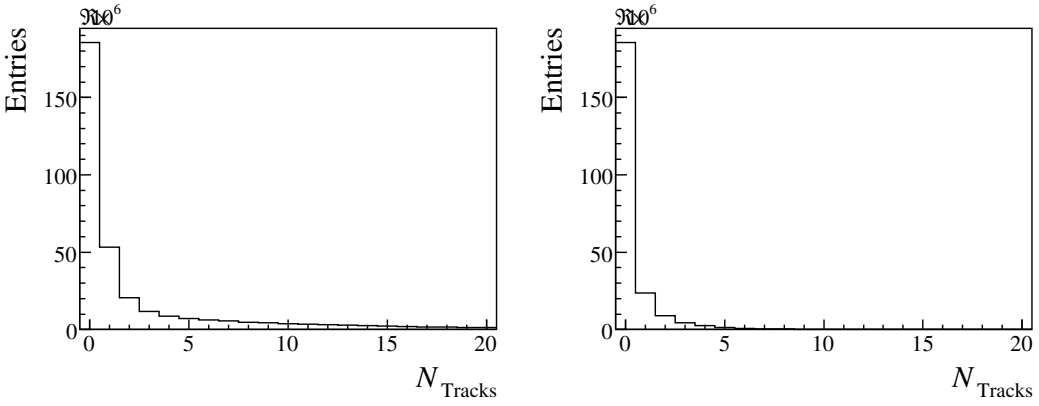

Figure 5.7: The number of V^0 candidates where the same `rtrack` appears as daughter track. The effect is larger for the loose set of cuts CM (left) than for the stricter cuts CO (right).

resolution of the measurement is limited, the true candidate may be removed by this process. In a refinement of this analysis, other criteria should be tested for the cleaning procedure. It has been verified, that the simulation is able to correct for signal loss through this method.

5.3 Signal Extraction

The invariant mass has been calculated for all V^0 candidates during the reconstruction (see Section 4.2). In the analysis, it is collected in y-p_T bins for the candidates accepted

by the cuts. The calculation of the invariant mass and the parametrisation of the phase space are explained in Appendix B. To determine the number of real V^0 particles observed in each bin, the background is subtracted from the resulting histograms by a fit. The fit-function consists of one part to describe the background and another one for the invariant mass peak.

The form and the amount of the background vary a lot between the different bins. The cuts that preserve the signal at high p_{T} lead to an enormous amount of background at low p_{T}. Other, stricter cuts provide practically background-free mass peaks. The background function has to adapt itself to all of these different conditions. Here a polynomial of degree 4 proved to be the most stable solution to fit the $\mathrm{K}^0_{\mathrm{S}}$ background. The more curved background for the Λ proved to be best fitted by a polynomial of degree 7. The addition of an exponential term can help to describe the onset of the background at a threshold defined by the sum of the daughter particles masses: $m_{\mathrm{threshold}} = m_1 + m_2$. With no combination, an invariant mass below this threshold can be constructed. The resulting fit function for the background is is

$$f_{\mathrm{Bg}}\left(m_{\mathrm{inv}}\right) = \left(1 - \exp\left(-\frac{m_{\mathrm{inv}} - m_{\mathrm{threshold}}}{\alpha}\right)\right) \cdot \sum_{i=0}^{n} a_i m_{\mathrm{inv}}^i$$

with α and the polynomial coefficients a_i as free fit parameters; n is the degree of the polynomial.

The shape of an invariant mass peak can be described by the Breit-Wigner distribution (Lorentz curve):

$$f_{\mathrm{Lorentz}}\left(m_{\mathrm{inv}}\right) = \frac{a \cdot \Gamma^2}{4\left(m_{\mathrm{inv}} - m_0\right)^2 + \Gamma^2}$$

where a is a fit parameter, Γ the full width at half maximum and m_0 the nominal particle mass and the centre of the distribution. If left free, m_0 reproduces the nominal value [34]. The measured width Γ is not determined by the natural line width of the decay, but by the resolution of the momentum and the V^0 decay vertex postion measurement. It is thus depending on the phase space. While the natural line widths are $\Gamma_\Lambda = 2.5$ eV/c^2 and $\Gamma_{\mathrm{K}^0_{\mathrm{S}}} = 7.4$ eV/c^2, respectively, a fit of the peaks with the Lorentz curve yields widths in the range of 5 MeV/$c^2 \leq \Gamma \leq 30$ MeV/c^2, depending on the location in phase space. The description of the peak by the Lorentz curve is fair, only overestimating the tails of the distribution. A better approach is to use the peak shape obtained from the simulation in the same y-p_{T} bin instead as the function f_{Pk} describing the peak.

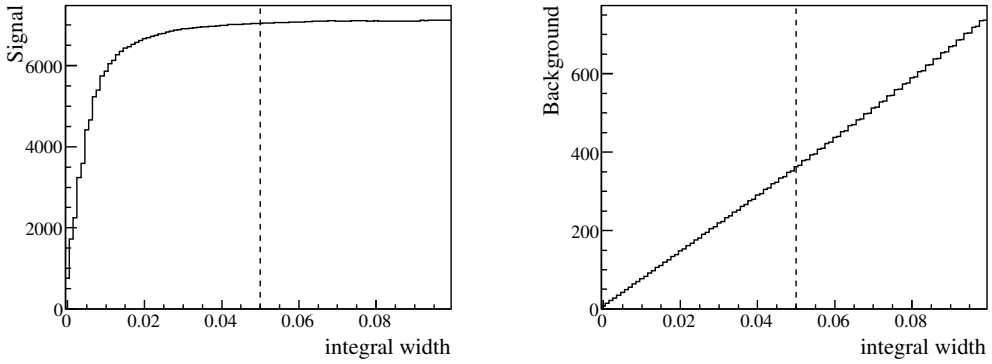

Figure 5.8: Dependence of the integrated signal (left) and background (right) on the integral width (for K^0_S). The line indicates the chosen value of 50 MeV.

It perfectly reproduces the form of the measured mass peak and only needs one fit parameter for scaling the height compared to three in the Lorentz curve. This makes the fit faster and more stable.

Fitting is carried out with the MINUIT package in ROOT (see Section 4.3) through a χ^2 minimisation while varying the parameters. Here, it is done in two steps: First, the background is fitted only by f_{Bg}, with the peak region being excluded. The parameters found by this step are then taken as start parameters for the fit to the whole histogram with $f_{\mathrm{Bg}} + f_{\mathrm{Pk}}$. Now, the background can be described by f_{Bg} with the parameters resulting from the second fit.

The signal is extracted by integrating over the histogram that contains the measured signal and background and subtracting the integral of f_{Bg}. The range of these integrals was chosen large enough to accept most of the true particles in all phase space regions. On the other hand it should not be chosen bigger than necessary, as a window that is too large raises the statistical error on the background. A compromise was found by studying the dependence of signal and background on this integration width throughout the phase space. This is illustrated for one y-p_T bin in Fig. 5.8. The resulting values are 50 MeV for K^0_S and 7.5 MeV for Λ. A verification in the simulation proved that less than 10% of the true V^0 particles are rejected by this cut in every y-p_T bin. The fit results for some arbitrarily chosen phase space bins are shown in Fig. 5.9. The comprehensive collection of invariant mass spectra is presented in Appendix A.

The signal decreases exponentially with p_T, making the fit more difficult at high p_T. Where the background is low as well, a different signal extraction method is possible.

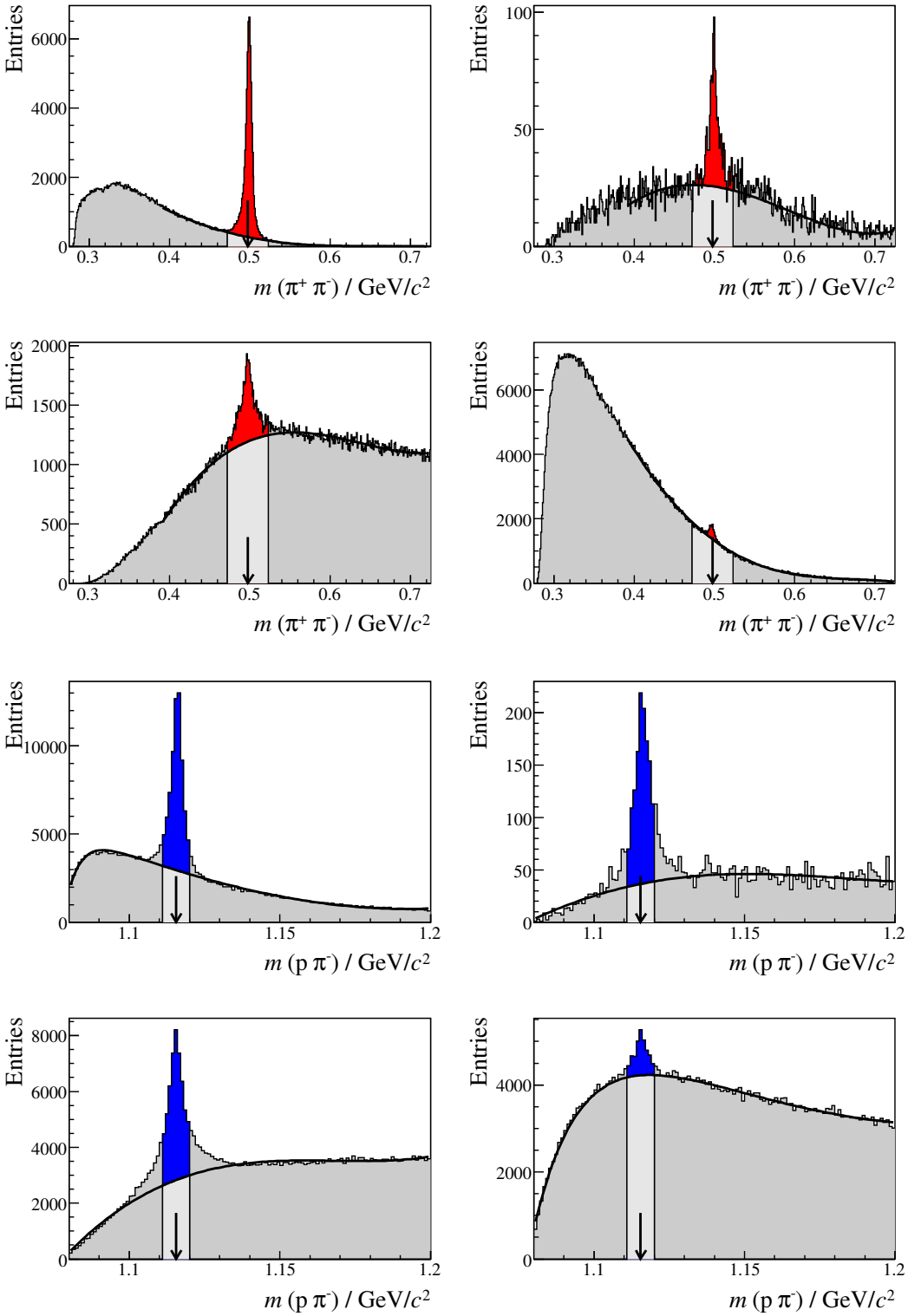

Figure 5.9: Examples for invariant mass spectra from different phase space bins together with the result of the fit. The four upper panels are from the $\mathrm{K}^0_{\mathrm{S}}$ analysis while the lower four are for Λ. The coloured region corresponds to the signal that is extracted. An arrow indicates the nominal mass. All Fit results are given in Appendix A.

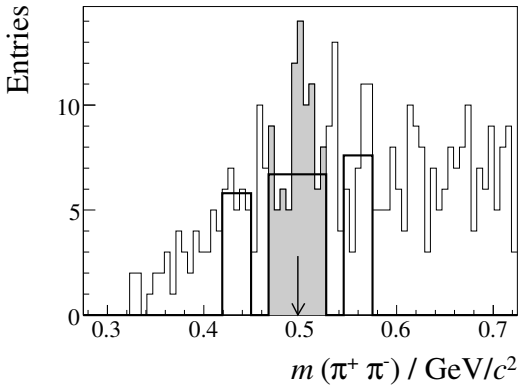

Figure 5.10: Signal extraction at high p_T. As an example, the invariant mass spectrum for K^0_S in the interval $2.41 \leq y \leq 2.91, 3.4\text{GeV}/c \leq p_T \leq 3.6\text{GeV}/c$.

Instead of the polynomial background fit, a linear extrapolation was used where the fit has problems due to low statistics. Therefore, the entries in defined bands on both sides outside of the peak region are counted and subtracted from the integral in the peak region. This method is visualised in Fig. 5.10. It agrees with the fit results. For the spectra presented in the following, only the fit method was used. But a minimum number of entries in the mass peak region was required. Where this is not reached, no signal can be extracted with either method.

Systematic Error

Through the utilisation of the mass peak from the simulation in the fit, a very good description of the invariant mass spectra is achieved. Nevertheless, a variation of the degree of the polynomial describing the background leads to different results where it is not possible to tell which one describes the background best. Figure 5.11 shows the comparison of the fit results for one phase space bin. These differences are concentrated in the domain where the background is high. In the transition region, where both methods can be used, the linear background extrapolation used at high p_T was also compared to the fit results. Differences between signal extraction methods are always below 5%. Thus, an overall systematic uncertainty of 5% can be estimated to emerge from the signal extraction procedure.

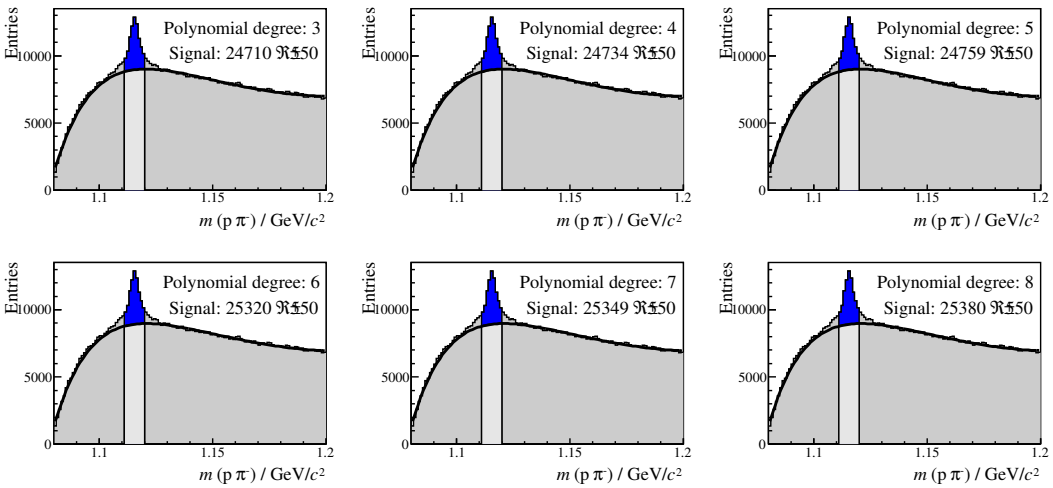

Figure 5.11: Check for the stability of the fit method for one example Λ invariant mass spectrum.

5.4 Acceptance and Efficiency Correction

By extracting the measured signal in each y-p_T bin with the procedure described above, raw particle spectra can be produced. To correct these for geometrical acceptance and reconstruction efficiency, embedding of simulated particle tracks is done differentially. The simulation chain that is used is described in Section 4.4.

The first step is the Monte Carlo generation of particles. Values for y, p_T and ϕ were randomised according to predefined distributions. For y, a Gaussian distribution with the mean width of the charged kaon spectra was used for K^0_S, while for Λ the sum of three Gaussians was used that reproduces the Λ rapidity distribution measured in [32]. Although this does not reflect the natural spectra, a uniform distribution in p_T was generated since this allows to achieve enough statistics for the correction at high p_T. The ϕ spectrum was chosen to be flat like in nature.

In GEANT, the particle properties are modified in such a way that all simulated particles decay into the charged channels which can be measured. These decay channels are listed in Table 4.1 on page 34. The measured spectra as well as the correction factors are for these channels only. As the decay mode is not correlated with other particle properties, it suffices to multiply the final spectra with the inverse of the branching ratios taken from [34] in order to get the final yield. After being processed through the simulation by GEANT and MTSIM, ten generated particles are embedded into the same

event. Therefore, 245 events from different runs were reused multiple times until a total of 2.55 M K^0_S and 2.26 M Λ were simulated.

All inefficiencies in the whole process of measurement, reconstruction and analysis have to be reproduced in the simulation. The detector effects are taken care of in GEANT and MTSIM. The inefficiencies of the reconstruction are automatically the same for embedded and normal events, as the same V^0 finder program is used. The analysis cuts have to be applied when examining the MC mini-DSTs in the same way as in the analysis of regular mini-DSTs before the search for matches can start. The cleaning procedure described in Section 5.2 is also applied on the MC data.

Like in the signal extraction procedure, a minimum number of entries was required here as well. Phase space regions, where the number of matched particles fails a threshold cannot be considered.

5.5 Cut Studies for K^0_S

As mentioned before, different sets of cuts have been compared in this analysis. One set of cuts that preserves the signal at high p_T and others to check the consistency of analysis and corrections. For three different cuts, the values are listed in Table 5.2. They are labeled CM, CC and CO, respectively. CM is the loosest set of cuts studied here. The high p_T spectra are derived from its results. The two other sets of cuts are for checking the consistency in the lower p_T range where also the stricter cuts retain a signal. The raw spectra, efficiency corrections and corrected spectra acquired with these cuts are compared in the following. The corrected spectra agree very well, although the cuts differ a lot. From the differences in the results, a systematic error is estimated.

Raw Spectra

The raw spectra for K^0_S are compared in Fig. 5.12. For $p_T \geq 0.4\text{GeV}/c$, the yield drops with increasing strictness of cuts. The loosest cuts, CM, yield the highest signal, but no large difference to CC is seen. CC only removes marginally more of the signal than CM. The set of cuts CO removes a significant part of the signal, leading to a lower spectrum ends because of a lack of statistics earlier than the others.

Cut	CM	CC	CO
$z_{\text{Vertex}} \leq$	-555.0 cm	-550.0 cm	-550.0 cm
Decay vertices inside sensitive volume excluded			
$\lvert x_{\text{Target}} \rvert \leq$	1.00 cm	0.50 cm	0.45 cm
$\lvert y_{\text{Target}} \rvert \leq$	0.50 cm	0.25 cm	0.20 cm
$\lvert \cos \Theta^* \rvert \leq$			0.75
Accepted candidates	52%	15%	3%
Mean efficiency	6.2%	6.0%	4.7%

Table 5.2: Different cut sets applied in the K^0_S analysis.

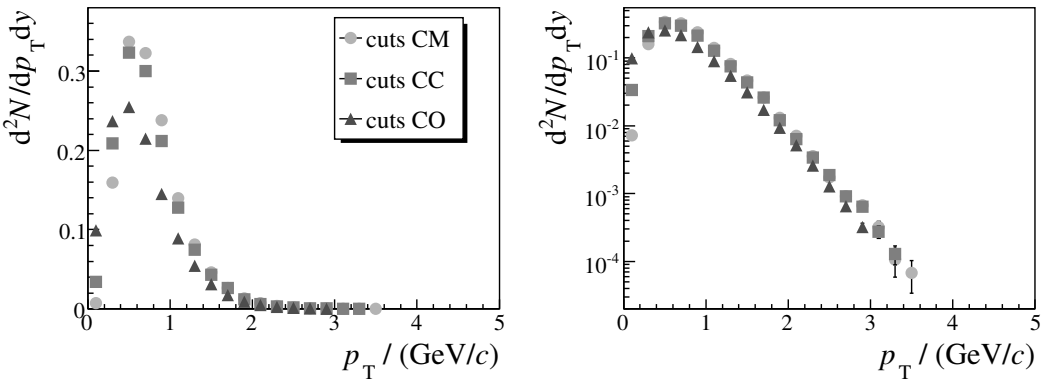

Figure 5.12: Comparison of K^0_S raw spectra at midrapidity ($-0.5 < y_{\text{CM}} < 0.5$) for different cuts. They are plotted with a linear (left) and a logarithmic scale (right) to make the differences in different p_T ranges visible.

Below $p_T = 0.4\text{GeV}/c$, the sequence of the raw spectra is reversed. The strictest cuts lead to the highest yields. It turns out that the effect of the "cleaning" procedure (see Section 5.2) is much stronger for the loose cuts here, removing a considerable part of the signal as well.

The signal over background ratio shown in Fig. 5.13 reflects the cut properties. The looser cuts CM and CC lead to a large background while the set CO considerably suppresses the background. But the signal vanishes earlier for CO than for the other two.

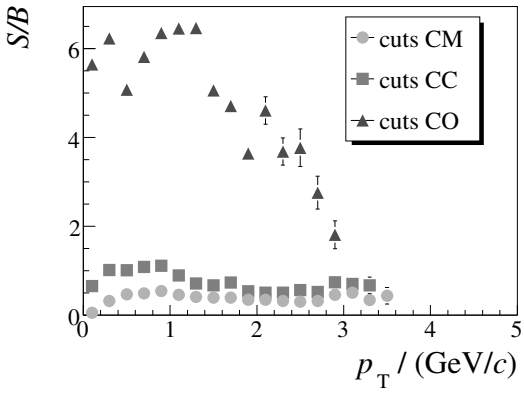

Figure 5.13: p_T dependence of the K^0_S signal over background ratio at midrapidity ($-0.5 < y_{CM} < 0.5$) for different cuts.

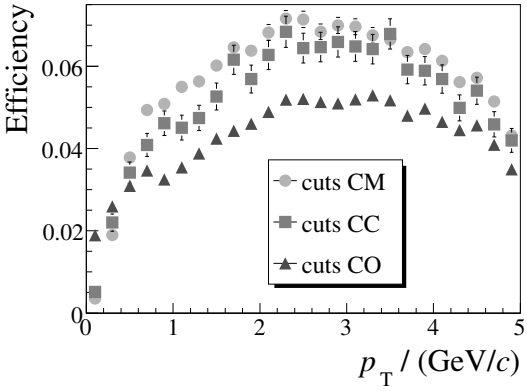

Figure 5.14: p_T dependence of K^0_S efficiency at midrapidity ($-0.5 < y_{CM} < 0.5$) for different cuts.

Efficiency Corrections

The efficiencies acquired from the simulation (shown in Fig. 5.14) reproduce the effect of the cuts and the "cleaning" procedure on the signal. While for $p_T \geq 0.4\text{GeV}/c$ the efficiency drops when applying stricter cuts, the order is reversed for lower p_T.

Corrected Spectra and Systematic Errors

The spectra presented in Fig. 5.15 are gained by correcting the raw spectra for the efficiency of the corresponding set of cuts and for the branching ratio (see Section 5.4). They agree for the compared cuts within 10%.

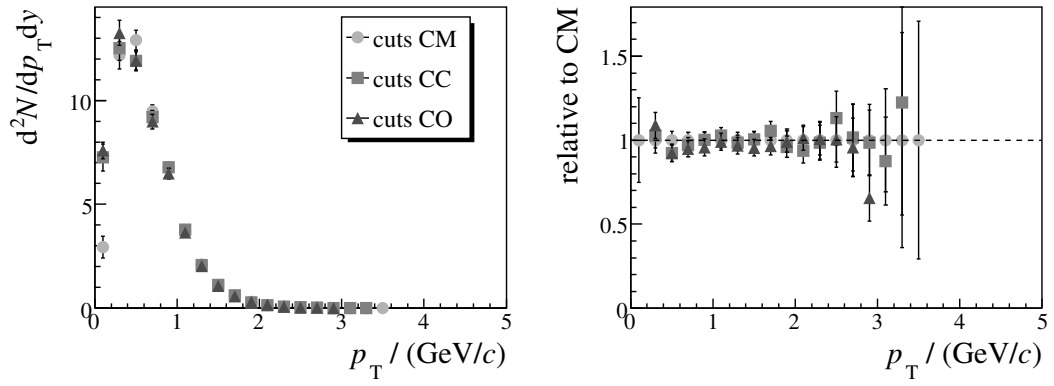

Figure 5.15: Comparison of corrected K^0_S spectra at midrapidity ($-0.5 < y_{CM} < 0.5$) for different cuts.

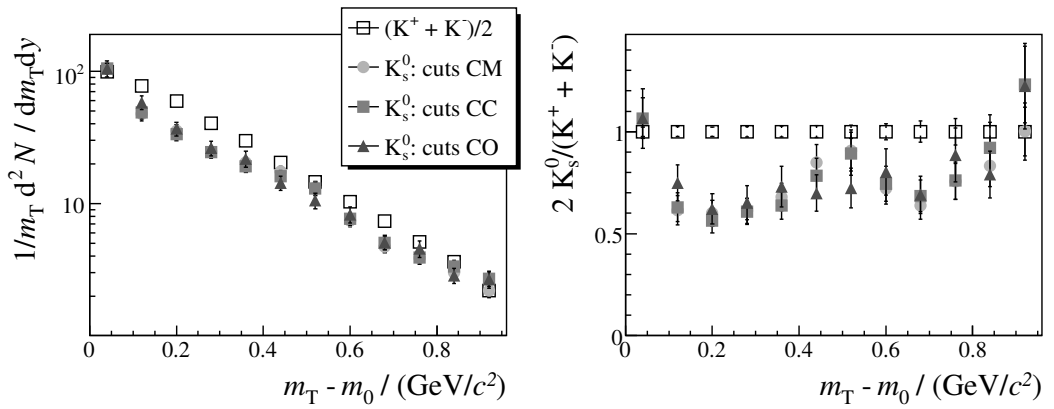

Figure 5.16: Comparison of the corrected K^0_S spectra at midrapidity ($-0.1 < y_{CM} < 0.1$) for different cuts with the $K^{\pm}$ spectra from [42]. The K^0_S results have been scaled for the difference in centrality between the two analyses.

While the analysis has been checked to be self-consistent, a discrepancy remains when comparing the measured values for neutral kaons to the results of the charged kaon analysis published in [42]. This is depicted in Fig. 5.16. A difference of 40% can be seen for small $m_T - m_0$, but it seems to get weaker for $m_T - m_0 > 0.7$ GeV/c^2. No published data is available for comparison at even higher transverse masses.

This comparison has to be taken with caution in any case: The theoretical implication that $\langle K^0_S \rangle = 1/2\,(\langle K^+ \rangle + \langle K^- \rangle)$ is only valid for 4π yields in isospin-symmetric systems. But the K^0_S spectra shown in Fig. 5.16 as well as the values for charged kaons stem from the rapidity interval $-0.1 < y_{CM} < 0.1$. Another problem in the comparability is that the $K^\pm$ analysis is based on a dataset containing only the 5% most central interactions. The system size dependence of charged kaons roughly follows a wounded nucleon scaling [43]. The K^0_S spectra extracted from the 23.5% most central events have therefore been scaled by the corresponding numbers of wounded nucleons ($\langle N_W \rangle = 357$ for 5% and $\langle N_W \rangle = 267$ for 23.5%).

A possible explanation for the discrepancy may be problems resulting from the high beam intensity used to record the high statistics sample used in this analysis. A detailed description of this problem is given in Section 5.7.

5.6 Cut Studies for Λ

Two sets of cuts were compared for the Λ. The first, CM, is loose enough to allow the observation of the signal up to $p_T = 3.8$ GeV/c. It is compared to the results of the set CC, which is stricter. NM and NC represent the same cuts, but here, the cleaning procedure described in Section 5.2 was not performed. This results in the signal vanishing in a huge background at low p_T. The used cut values are summarised in Table 5.3.

Raw Spectra

No large difference can be observed in the raw spectra (presented in Fig. 5.17) between the CM and CC cut sets. But it is clearly visible that the cleaning process has an effect on the signal, thus removes true V^0 particles from the candidate lists. At higher p_T, this difference vanishes, as here ambiguities only appear rarely and thus the cleaning procedure is hardly used. For all four approaches presented here, the background is large

Cut	CM/NM	CC/NC
$z_{\text{Vertex}} \leq$	-555.0 cm	-550.0 cm
Decay vertices inside sensitive volume excluded		
$\lvert x_{\text{Target}} \rvert \leq$	1.00 cm	0.50 cm
$\lvert y_{\text{Target}} \rvert \leq$	0.50 cm	0.25 cm
Accepted candidates	53%	15%
Mean efficiency	4.0%	3.7%

Table 5.3: Different cut sets applied in the Λ analysis. CM and CC denote an analysis with application of the "cleaning" procedure (see Section 5.2) while NM and NC refer to the same cuts without cleaning process.

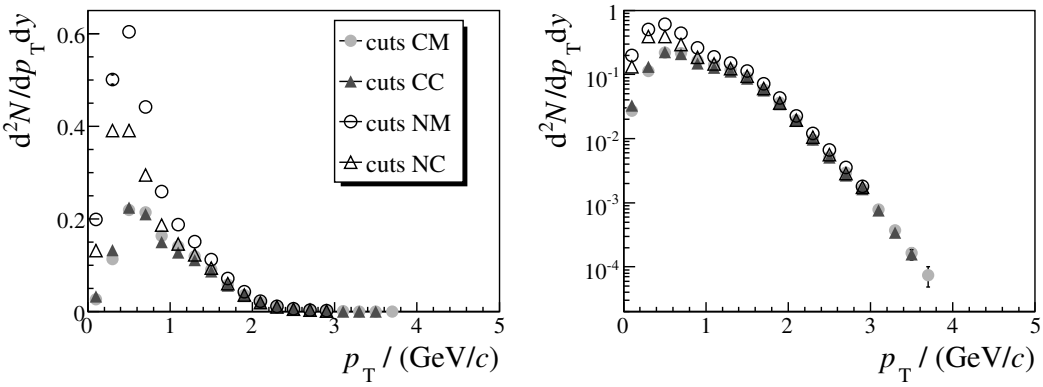

Figure 5.17: Comparison of Λ raw spectra at midrapidity ($-0.5 < y_{\text{CM}} < 0.5$) for different cuts. They are plotted with a linear (left) and a logarithmic scale (right) to make the differences at low and high p_T visible.

at low p_T, and the signal/background ratio (see Fig. 5.18) is very low there. But for NM and NC, it is so low, that the systematic error in the signal extraction (see 5.3) exceeds the limit of 5% for $p_T < 0.6$ GeV/c. Figure 5.19 shows the invariant mass spectrum for $0.0 < y_{\text{CM}} < 0.5$, 0.0 GeV/$c$ $< p_T <$ 0.2 GeV/c. The fit fails and the resulting yield is too large.

Efficiencies and Corrected Spectra

The efficiencies of the four methods compared are depicted in Fig. 5.20. The impact of the cleaning procedure is evidently reproduced by the simulation. The effect of the

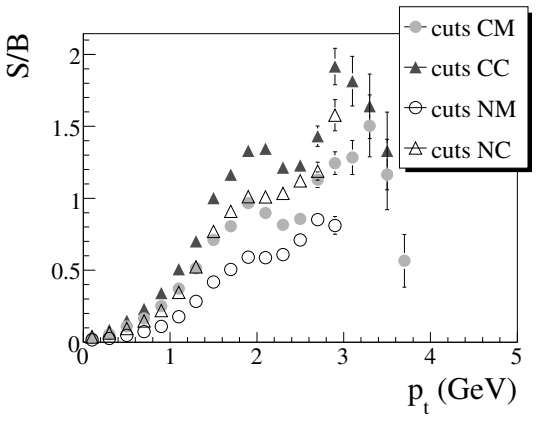

Figure 5.18: p_{T} dependence of Λ signal over background ratio at midrapidity ($-0.5 < y_{\mathrm{CM}} < 0.5$) for different cuts.

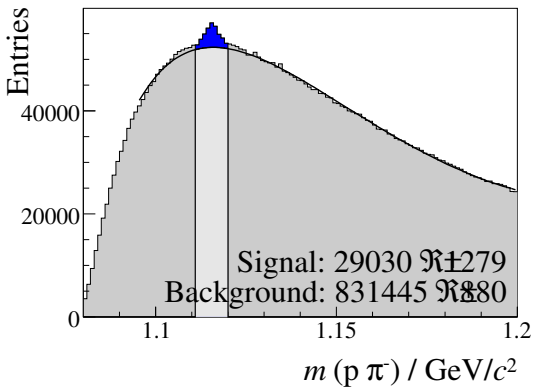

Figure 5.19: Λ invariant mass spectrum for $0.0 < y_{\mathrm{CM}} < 0.5$, 0.0 GeV/$c$ < $p_{\mathrm{T}} < 0.2$ GeV/c. The fit fails to describe it in this phase space interval.

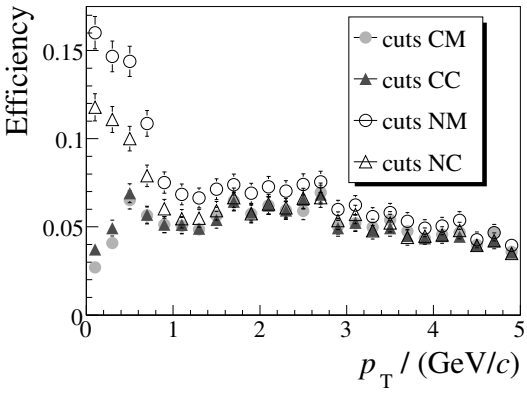

Figure 5.20: p_{T} dependence of the efficiency for Λ at midrapidity ($-0.5 < y_{\mathrm{CM}} < 0.5$) for different cuts.

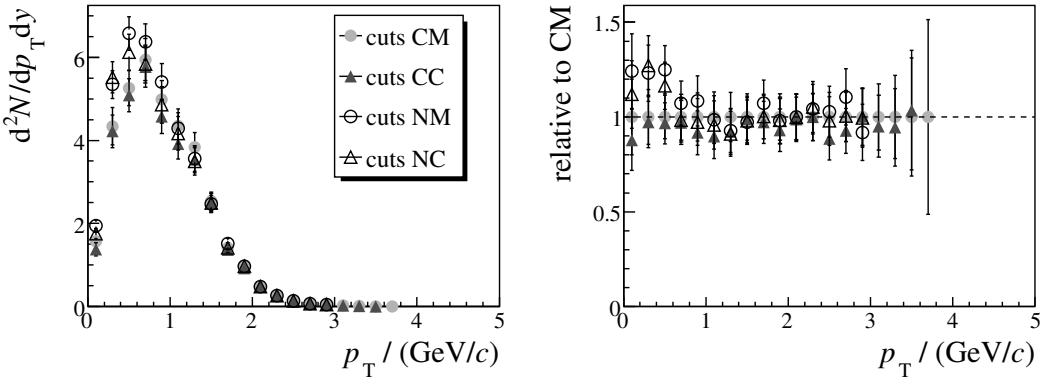

Figure 5.21: Comparison of corrected Λ spectra at midrapidity ($-0.5 < y_{\mathrm{CM}} < 0.5$) for different cuts.

cleaning on the signal is less pronounced for the stricter cuts, what can be seen in the differences in efficiency being larger between CM and NM than between CC and NC.

The agreement of the corrected spectra between the four methods that were compared is good, an exception is the low p_{T} region for NM and NC. This discrepancy can be explained by the uncertainty of the signal extraction procedure in this phases space region that is caused by the huge background there.

Systematic Errors

The low p_T region for the NM and NC variants cannot be considered when estimating the systematic error, as the signal extraction fails here. Disregarding these points, the different approaches agree well and a systematic error of 10% can be assumed.

Figure 5.22 shows an exponential fit to the corrected Λ spectrum. This fit has the form

$$\frac{\mathrm{d}^2N}{\mathrm{d}p_T\mathrm{d}y} = C \cdot p_T \cdot e^{-m_T/T}$$

and thus implies thermal particle emission. It has therefore only been fitted in the low p_T region, as no exponential spectrum can be expected above. The points below $p_T = 0.6$ GeV/c have also been excluded due to the systematic error in the signal extraction there. Nevertheless, the fit meets them quite well.

The midrapidity yield extracted from the spectrum by integrating the bin contents is $\mathrm{d}N/\mathrm{d}y|_{|y|<0.5} = 7.5 \pm 0.9$. It can be compared to the results from an earlier analysis of Λ production in Pb+Pb collisions at 158 A GeV [44]. Like for the kaon check (see Section 5.5), the difference in centrality between the two datasets analysed has to be compensated by a number of wounded nucleons scaling. The results in [44] stem from the 10% most central collisions, according to $\langle N_W \rangle = 335$.

After the scaling, the value for the analysis presented in this thesis amounts to 9.4 ± 1.1, which agrees within errors with the value of $\mathrm{d}N/\mathrm{d}y|_{|y|\leq 0.4} = 10.9 \pm 1.0 \pm 1.3$ published for the more central analysis. The inverse slope parameter $T = 295 \pm 6$ MeV extracted from the fit agrees very well to the published value $T = 304 \pm 16 \pm 23$ MeV.

5.7 Open Issues

In the course of this analysis, not all effects on the results could be clarified. Two issues remain unsettled, they are discussed in this section and possible solutions are suggested.

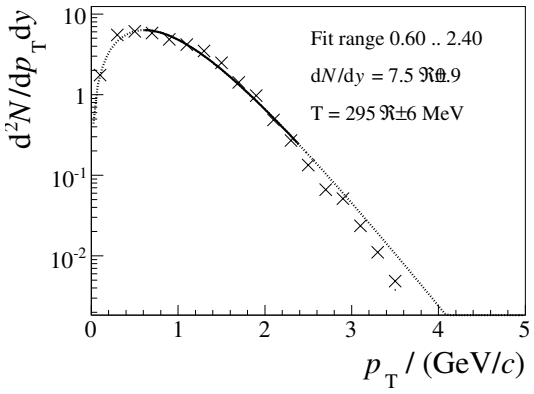

Figure 5.22: Exponential fit to the corrected Λ spectrum at midrapidity ($-0.5 < y_{\mathrm{CM}} < 0.5$).

Feeddown Correction

This analysis does not explicitly distinguish between primary V^0 particles that have been produced at the main vertex, and secondary particles stemming from decays. While no noteworthy source of secondary $\mathrm{K}^0_{\mathrm{S}}$ is known, secondary Λ arise from the decay of Ξ.

All Λ that fulfill the cut criteria and that are counted in the signal extraction process are included in the spectra. To obtain the corresponding yields of primary Λ, a *feeddown correction* would be required. It has been estimated in earlier analyses ([31], [32]) that the feeddown contribution from Ξ^- and $\overline{\Xi}^0$ is between 4% and 5%. But only a simulation process similar to that conducted for the efficiency correction can provide the fraction of secondary Λ falling into the acceptance differentially in all regions of phase space. This has not been done in this analysis yet.

Influence of δ Electrons

A possible explanation for the discrepancies between charged and neutral kaons is an effect caused by the high beam intensity that was used to record the data sample on which this analysis is based (see Section 3.4). It was not yet possible to find a concluding solution for this problem.

The Wave Form Analyser (WFA) collects information from the beam counters to determine the number of beam particles (N_{Beam}) that traverse the detector during TPC readout. $N_{\mathrm{Beam}} = 1$ corresponds to the ideal situation where only one Pb ion that

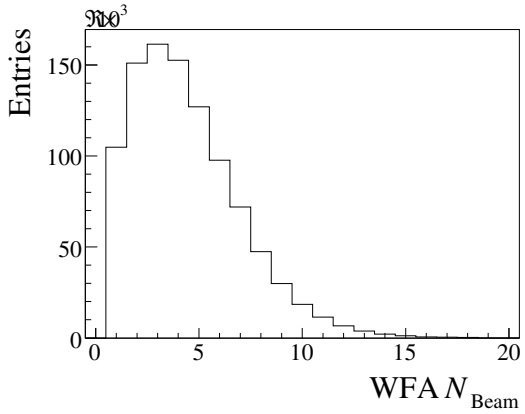

Figure 5.23: N_{Beam} distribution for the central Pb+Pb 2000 dataset.

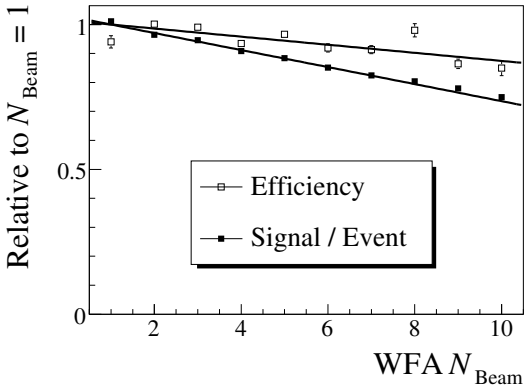

Figure 5.24: The relative dependence of the $\mathrm{K}^0_{\mathrm{S}}$ raw signal and the efficiency on N_{Beam}.

interacts in the target is present. Events with more than one inelastic interaction in the target during this time window are excluded, but additional beam particles that do traverse the target without inelastic interaction can release δ electrons through elastic interaction with the target or the detector gas. These electrons feature low momenta of $\approx$ 0.2 GeV/c and thus cause spiral tracks with a small curvature radius. The reconstruction efficiency might be worsened by them.

The N_{Beam} distribution for the dataset this analysis is based on is shown in Fig. 5.23. Its mean value is $\langle N_{\mathrm{Beam}} \rangle = 4.4$, only approximately 10% of all events possess a value of $N_{\mathrm{Beam}} = 1$. For low intensity run periods, the mean value is between 1 and 2 [45].

Figure 5.24 shows the dependence of the $\mathrm{K}^0_{\mathrm{S}}$ raw signal and the efficiency on N_{Beam} together with a linear fit. Both are normalised to the fit value for $N_{\mathrm{Beam}} = 1$. They

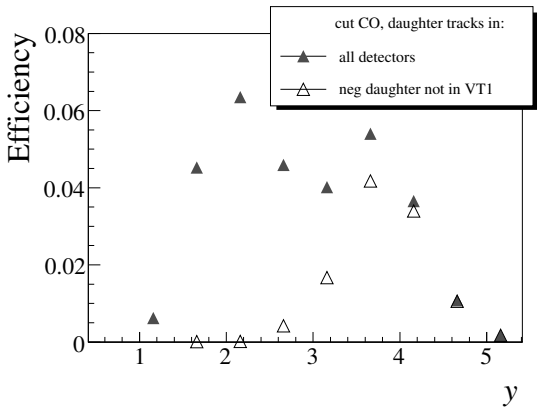

Figure 5.25: Rapidity dependence of efficiency for K^0_S for cuts on the detectors hit by the daughter particles.

show the same trend. Yet while the signal strictly follows the linear decrease, the values for the efficiency show more fluctuation. As well, the slopes differ.

This difference raises the question whether the simulation correctly reproduces the influence of N_{Beam}. But it might as well just be a problem of statistics: in the embedding process, the same 245 raw data events have been used again and again, and the spectrum of δ electrons contained in them might not be characteristic for the whole dataset. To clarify this question, a larger number of different events must be used as a basis for embedding.

In case that the effect of N_{Beam} should prove to be irreproducible in the simulation, a strategy has to be found that eludes this effect by avoiding the affected domains. But limiting the dataset to the $N_{\mathrm{Beam}} = 1$ events rejects 90% of the statistics. This is not acceptable in the search for rare probes like the signal at high p_T. One can assume that δ electrons mainly appear in VTPC1. Excluding V^0 particles from the analysis that have daughter tracks in this detector has a large impact on the efficiency at backward and mid rapidity (as shown in Fig. 5.25). More investigation is necessary to find out which cuts are suitable for this purpose.

Chapter 6

Results and Discussion

The $\Lambda/\ \mathrm{K}^0_\mathrm{S}$ ratio calculated from the spectra that result from the analysis presented in the previous chapter is shown in Fig. 6.1. It shows a saturation for $p_\mathrm{T} \geq 2$ GeV/c, making a description through hydrodynamical models impossible in this domain. The shape of the ratio is in qualitative agreement with observations made at RHIC.

Figure 6.2 shows parts of NA49's high p_T results presented at the Quark Matter 2005 conference [10]. The p/π^+ ratio shows a similar behaviour as the $\Lambda/\mathrm{K}^0_\mathrm{S}$ ratio. As the analysis procedure for charged particles is very different to the V^0 analysis, this can be seen as a confirmation by an independent analysis method. The measured $\Lambda/\mathrm{K}^0_\mathrm{S}$

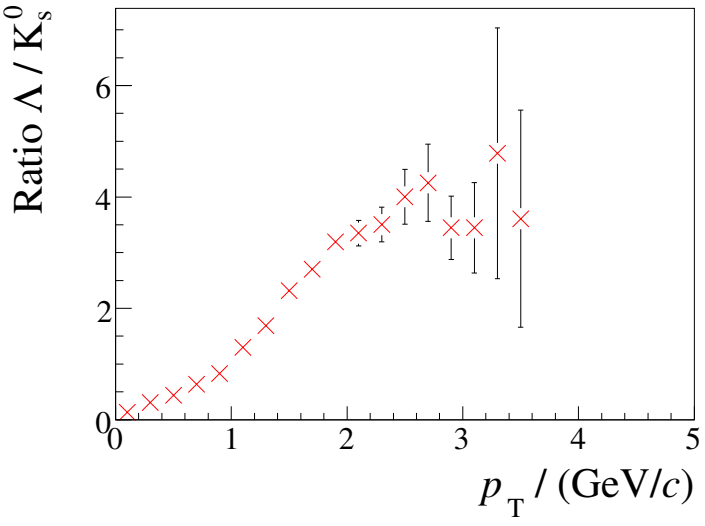

Figure 6.1: $\Lambda/\ \mathrm{K}^0_\mathrm{S}$ ratio for Pb+Pb collisions at 158 A GeV.

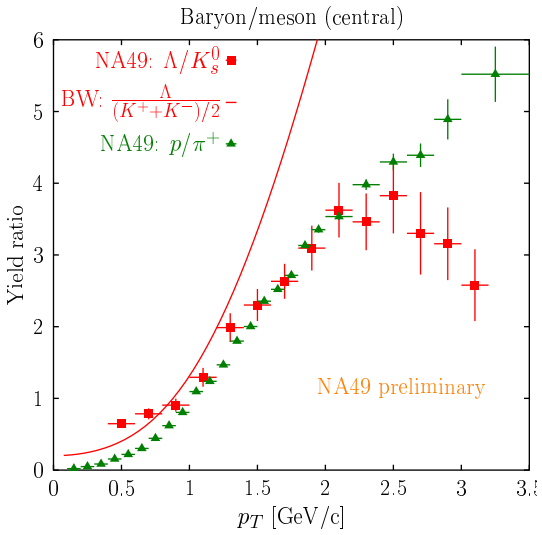

Figure 6.2: Baryon/meson ratios from NA49 compared to a blast wave (BW) model fit. The figure is taken from [10].

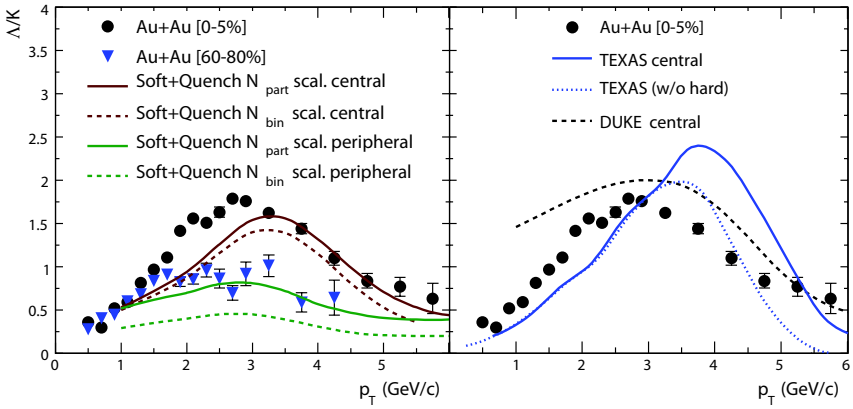

Figure 6.3: The $\Lambda/\mathrm{K_S^0}$ ratio as a function of p_T for central and peripheral Au+Au collisions at $\sqrt{s_\mathrm{NN}} = 200$ GeV, compared to coalescence models. The figure is taken from [8].

ratio is compared to a blast wave fit [46]. The blast wave parametrisation is a simple hydrodynamic model that describes low p_T spectra and freezeout parameters extracted from Bose-Einstein correlations simultaneously. It is in agreement with the ratio for $p_\mathrm{T} \leq 1.2$ GeV/c, but it fails for the high transverse momentum region.

No calculation from a coalescence model is available for the collision energy studied here ($\sqrt{s_\mathrm{NN}} = 17.3$ GeV). Nevertheless the comparison with RHIC data [8] suggests, that quark coalescence already plays a role at the SPS.

The unsettled question about the influence of δ electrons (adressed in Section 5.7) has to be clarified before a conclusion can be drawn from the spectra per se. On the other hand, for the presented yield ratio, systematic errors cancel out as they would equally affect the similar analyses for K^0_S and Λ.

Chapter 7

Summary

The motivation for studying ultrarelativistic heavy ion collisions is to search for signatures of a transition from hadronic matter to a partonic phase, the Quark-Gluon plasma. The bulk of the particles produced in these collisions possesses transverse momenta of $p_{\mathrm{T}} < 2$ GeV/c and evidence for the production of a Quark-Gluon plasma at SPS energies has been found in the properties of particles from this p_{T} range. The rare particles seen in the higher p_{T} domain can complete the picture of the produced matter. Examples for such high p_{T} signatures include the properties of the baryon/meson ratios and the elliptic flow in the region $2 < p_{\mathrm{T}} < 4$ GeV/c observed at RHIC. They can be explained by quark coalescence models.

This phase space range can also be accessed for analysis at the highest SPS beam energy of 158 A GeV. A study of the p_{T} dependence of baryon/meson ratios here can help to answer the question which hadron production mechanisms are relevant in this energy range. In the NA49 large acceptance hadron spectrometer, K^0_S and Λ are identified via the V^0 topology of their decay into charged hadrons and the determination of their invariant mass. The reach in p_{T} of this method is only limited by the statistics of the available data.

An important part of the analysis presented in this thesis is to select potential V^0 candidates by adequate cuts. Optimisation for the high p_{T} domain requires careful cuts in order to retain the signal there. A challenge implicated by this approach is the large combinatorial background left over by the loose cuts. A reliable signal extraction method was found that can deal with this possible difficulty and provide raw spectra. The fraction of particles that cannot be detected because of the geometrical acceptance

of the detector and analysis inefficiencies was determined in simulations. Correction factors are extracted from this simulation for each phase space bin and applied to the raw spectra.

The spectra corrected in this way reach $p_T = 3.6$ GeV/c (for K^0_S) and $p_T = 3.8$ GeV/c (Λ), respectively. The whole analysis method has been checked to be self-consistent and was compared to existing data on kaon and Λ production, that is only available in the lower p_T range. While the Λ spectra agree with an earlier analysis [44], a disagreement remains between the results for K^0_S presented here and charged kaon data published in [42].

The Λ/K^0_S ratio calculated from the corrected spectra qualitatively agrees with the results for the higher collision energy at RHIC [8]. A saturation of the ratio for $p_T \geq 2$ GeV/c clearly indicates that the hydrodynamical picture is not valid in the higher range any more. Unfortunately, no calculations from coalescence models are available for the SPS energy range so far.

Appendix A

Additional Figures

In the following, all invariant mass spectra used to produce the high p_{T} spectra are presented. The cut set CM was used for both $\mathrm{K}^0_{\mathrm{S}}$ and Λ. Midrapidity ($-0.5 < y_{\mathrm{CM}} < 0.5$) is covered and each spectrum is for a p_{T} interval of 0.2 GeV/c. In the left column, the spectra are shown as measured. A blue line indicates the fit to the whole spectrum, while a red line indicates the background fit. The background subtracted spectra are shown in the right column with a red line indicating the fit to the peak.

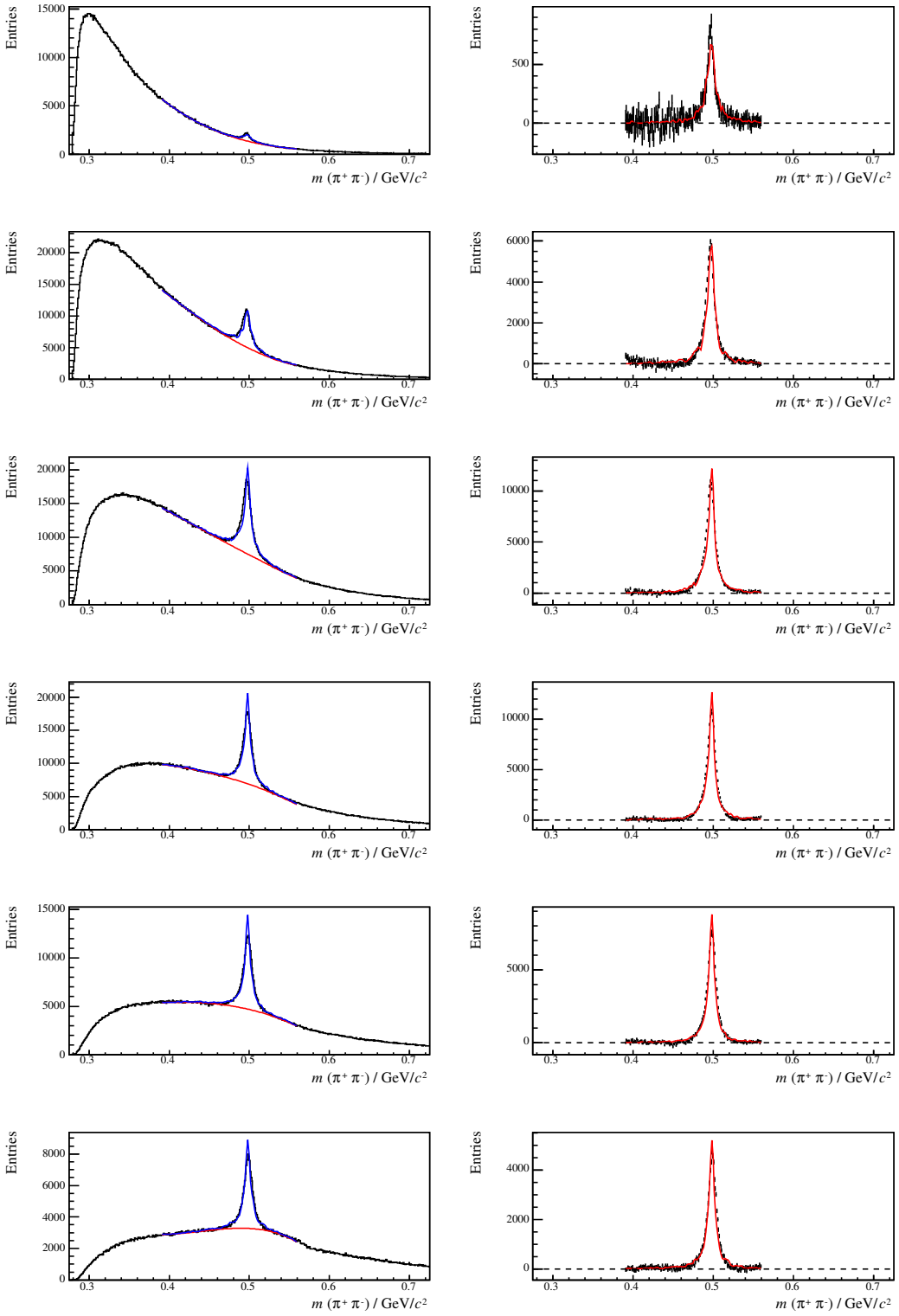

Figure A.1: The K^0_S invariant mass spectra for the CM cut set, in the range $-0.5 < y_{\mathrm{CM}} < 0.5$, 0.0 GeV/$c$ $< p_{\mathrm{T}} <$ 1.2 GeV/c.

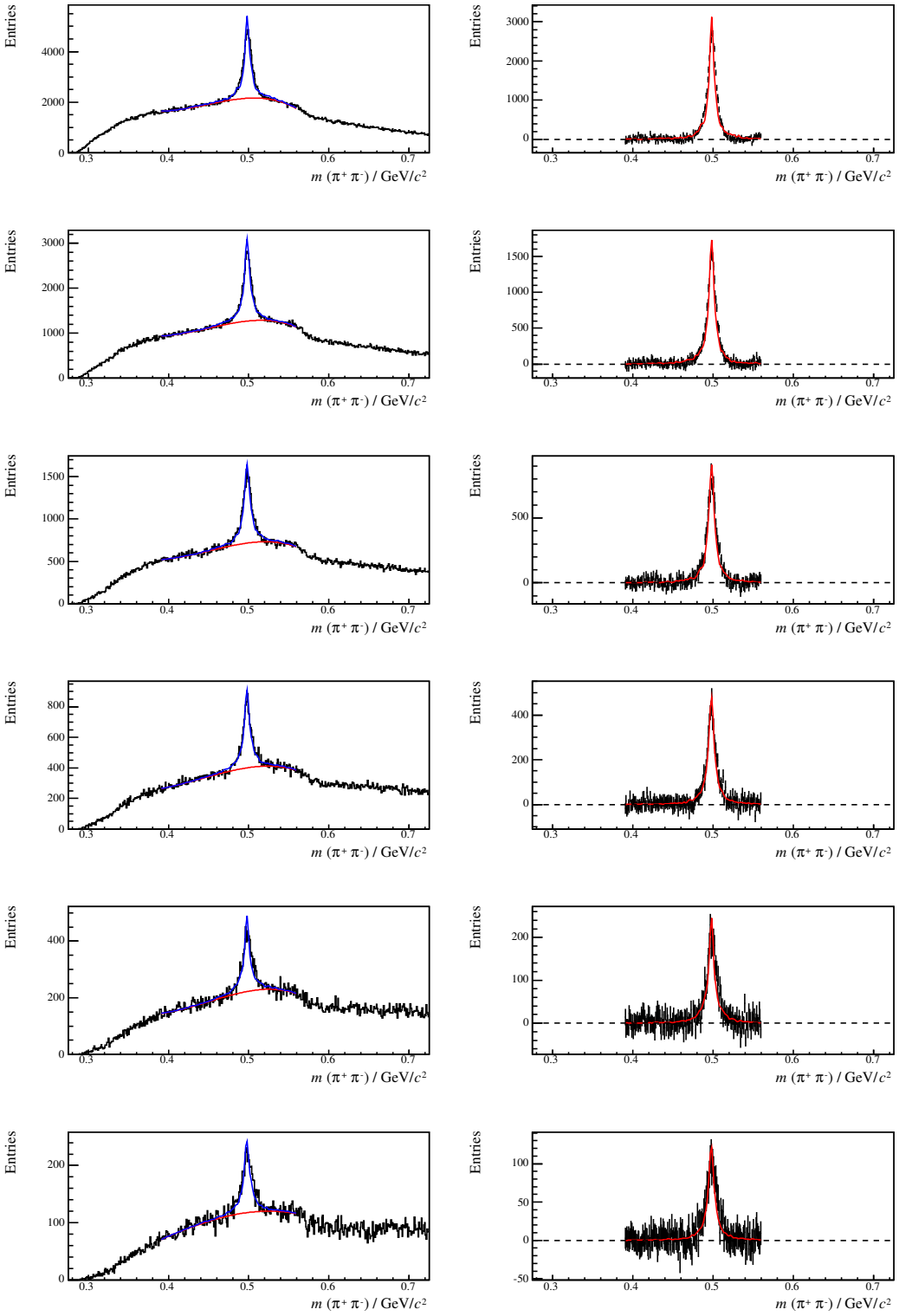

Figure A.2: The K^0_S invariant mass spectra for the CM cut set, in the range $-0.5 < y_{CM} < 0.5$, 1.2 GeV/c < p_T < 2.4 GeV/c.

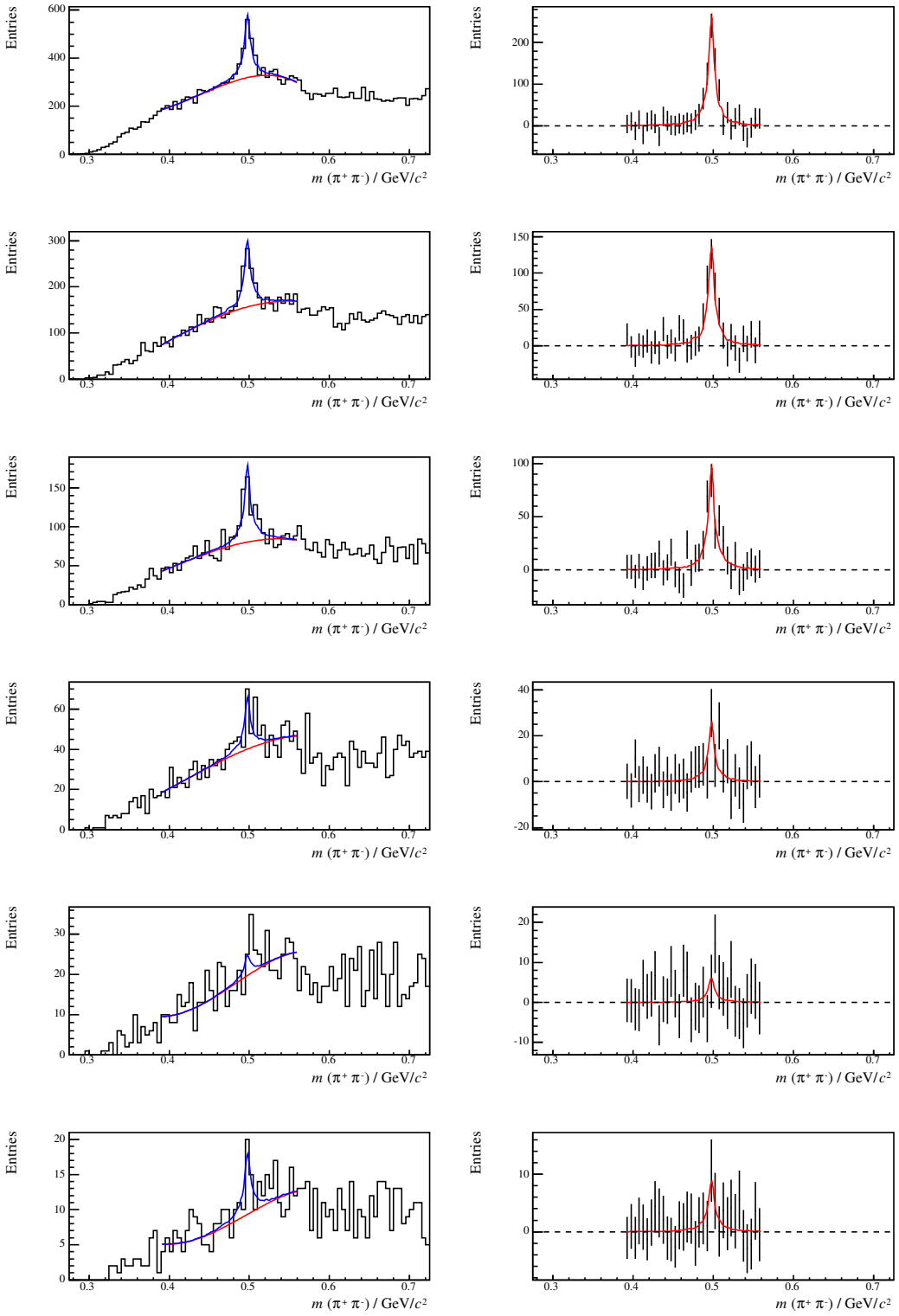

Figure A.3: The K^0_S invariant mass spectra for the CM cut set, in the range $-0.5 < y_{CM} < 0.5$, 2.4 GeV/c $< p_T <$ 3.6 GeV/c.

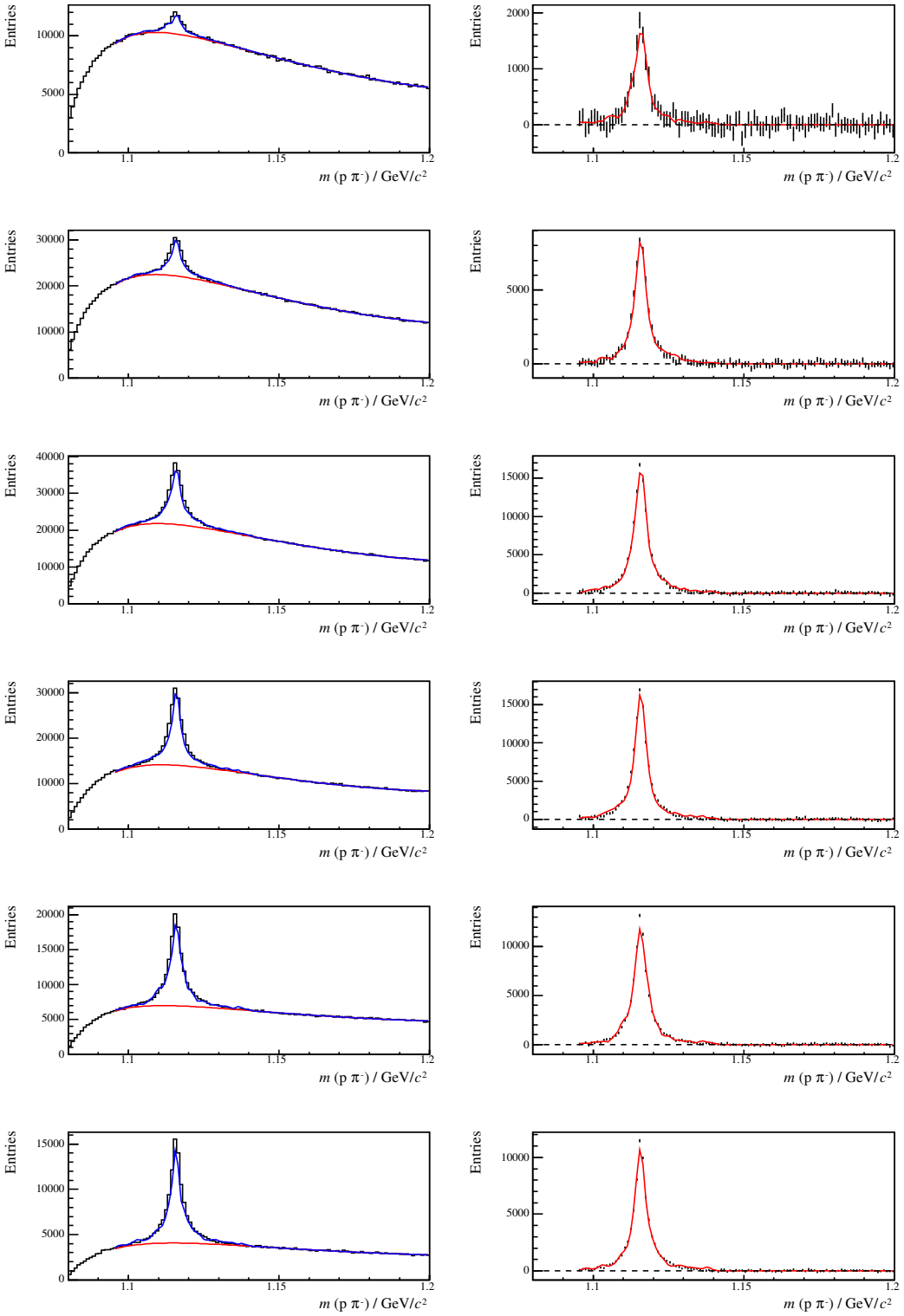

Figure A.4: The Λ invariant mass spectra for the CM cut set, in the range $-0.5 < y_{\mathrm{CM}} < 0.5$, 0.0 GeV/$c$ $< p_{\mathrm{T}} <$ 1.2 GeV/c.

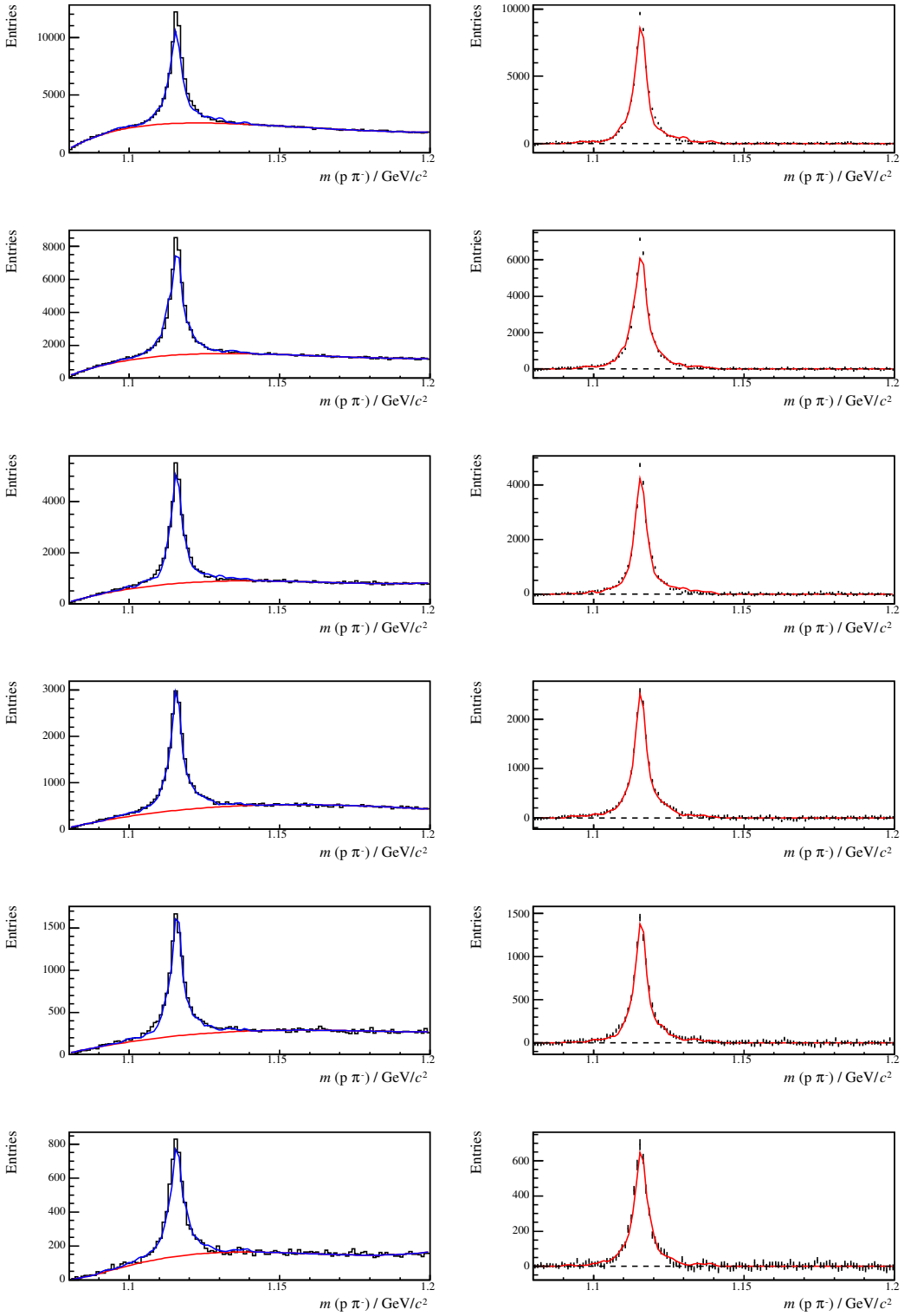

Figure A.5: The Λ invariant mass spectra for the CM cut set, in the range $-0.5 < y_{\mathrm{CM}} < 0.5$, 1.2 GeV/$c$ $< p_{\mathrm{T}} <$ 2.4 GeV/c.

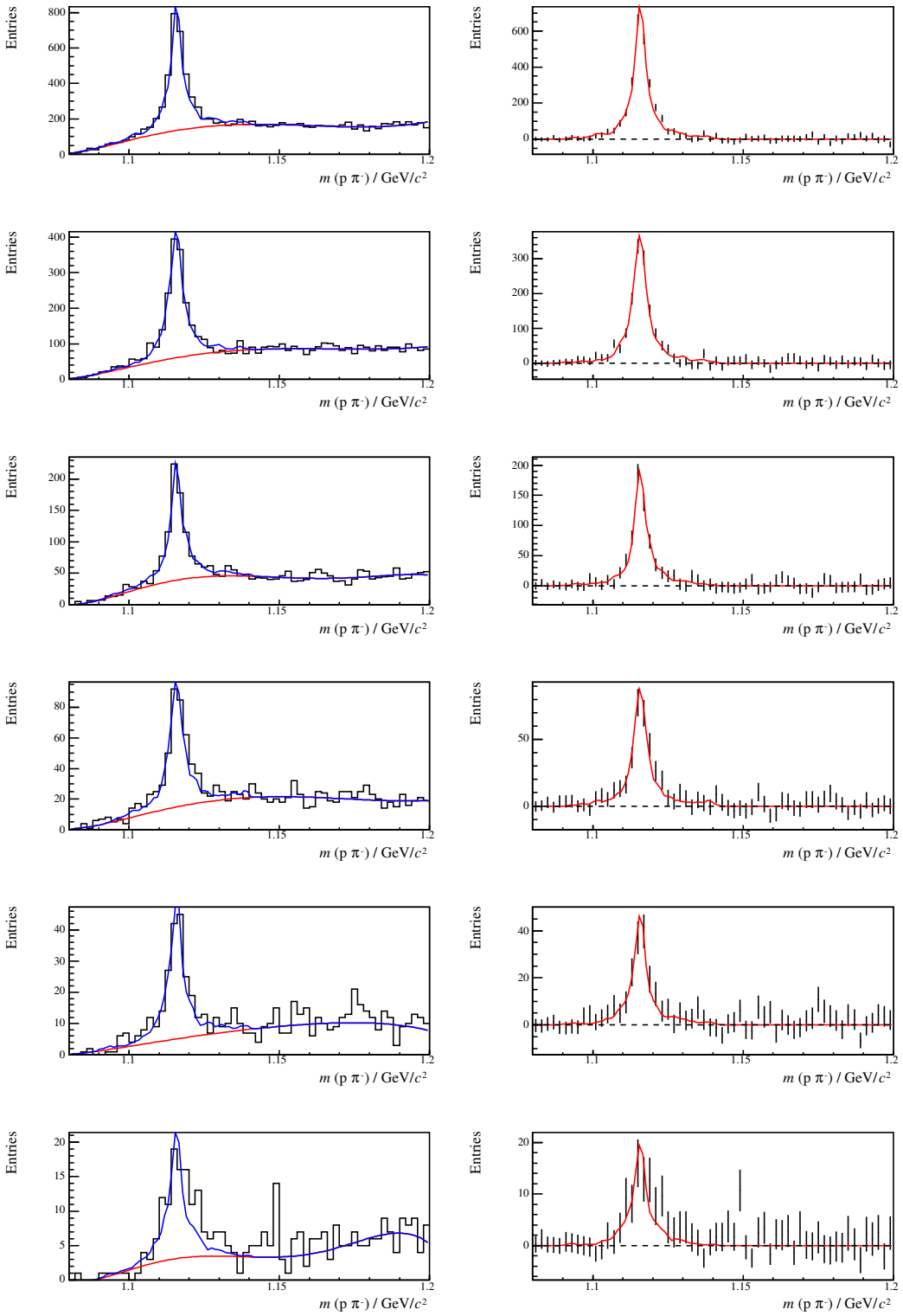

Figure A.6: The Λ invariant mass spectra for the CM cut set, in the range $-0.5 < y_{\mathrm{CM}} < 0.5$, 2.4 GeV/$c$ $< p_{\mathrm{T}} <$ 3.6 GeV/c.

h

Appendix B

Relativistic Kinematics

In the heavy ion collisions studied here, both initial and final state are highly relativistic, hence the name *ultrarelativistic heavy ion collisions*. The most important variables and units used are summarised in this chapter.

Considering time dilation or length contraction, the *Lorentz factor* γ is used. It is defined as

$$\gamma \equiv \frac{E}{m} = \frac{1}{\sqrt{1-\beta^2}} \tag{B.1}$$

where $\beta = v/c$ is the velocity expressed as fraction of the speed of light.

Units

The standard units used are GeV for energies, GeV/c for momenta, GeV/c^2 for masses and cm for lengths. While in the units c still appears, the convention $\hbar = c = 1$ is used for calculations.

Phase Space Variables of Final State

The phase space of the particles produced in the collisions is spanned by the three components of the momentum $\vec{p}$: p_x, p_y and p_z. It may be necessary to do Lorentz transformations along the beam (or z-) axis in order to change e.g. from the laboratory frame into the centre of mass system of the collision. In addition, the momentum

distribution in z is very broad (ranging from target to beam momentum) compared to the momenta perpendicular to the beam axis that only developed through scattering. This calls for different variables for *longitudinal* and *transverse* motion.

p_x and p_y are replaced by the *transverse momentum* p_T and the azimuthal angle ϕ by the following conversions:

$$\begin{aligned} p_\mathrm{T} &= \sqrt{p_\mathrm{x}^2 + p_\mathrm{y}^2} \\ \phi &= \arctan \frac{p_\mathrm{y}}{p_\mathrm{x}} \end{aligned} \tag{B.2}$$

When only the statistical properties of many events are considered, azimuthal symmetry can be assumed and ϕ does not play a role. Another important quantity is the *transverse mass*, defined as

$$m_\mathrm{T} \equiv \sqrt{p_\mathrm{T}^2 + m^2} \tag{B.3}$$

While the transverse momentum is Lorentz invariant under transformations along the beam axis, this is not the case for the longitudinal momentum p_z. It is therefore replaced by the *rapidity* denoted with y.

$$y = \frac{1}{2} \ln \left(\frac{E + p_\mathrm{z}}{E - p_\mathrm{z}} \right) \tag{B.4}$$

$E = \sqrt{|\vec{p}|^2 + m^2}$ is the particle's total Energy and m the mass. The rapidity is just linearly being shifted under Lorentz transformations and can alternatively be expressed as

$$y = \operatorname{arctanh} \beta_\mathrm{z}$$

where $\beta_\mathrm{z} = v_\mathrm{z}/c$ is the longitudinal velocity.

Invariant Mass Calculation

A particle's mass is invariant in any coordinate system. It can be expressed by

$$m = \sqrt{E^2 - |\vec{p}|^2} \tag{B.5}$$

In the V^0-decay, the mass m_V of the decayed particle can be reconstructed by using energy and momentum conservation in the decay. From equation B.5 then follows

$$\begin{aligned} m_\mathrm{V} &= \sqrt{(E_1 + E_2)^2 - |\vec{p}_1 + \vec{p}_2|^2} \\ &= \sqrt{m_1^2 + m_2^2 + 2\,(E_1 E_2 - \vec{p}_1 \vec{p}_2)} \end{aligned}$$

where E_i, $\vec{p}_\mathrm{i}$ and m_i are the energy, momentum and mass of the i-th daughter particle. The result depends on the assumption of the decaying particle, because the daughter particles' masses have to be put into the calculation. In the reconstruction, the invariant mass is calculated for any possible assumption.

Energies of Accelerators

The collisions in fixed target experiments are characterised by the beam energy. In order to make them comparable to Collider experiments, the energy disposable in the centre of mass frame is given per nucleon-nucleon pair:

$$\sqrt{s_\mathrm{NN}} = \sqrt{(E_\mathrm{Beam} + E_\mathrm{Target})^2 - |\vec{p}_\mathrm{Beam} + \vec{p}_\mathrm{Target}|^2}$$

At the highest SPS energy, where the beam energy per nucleon is $E_\mathrm{Beam} = 158$ GeV and the target is at rest ($E_\mathrm{Target} = 0$ GeV), the resulting centre of mass energy is $\sqrt{s_\mathrm{NN}} = 17.3$ GeV.

Appendix C

List of Used Abbreviations

ADC	Analog to Digital Converter
AFS	Andrew File System
API	Application Programming Interface
BNL	Brookhaven National Laboratory, NY, USA
BPD	Beam Position Detector
CASTOR	CERN Advanced STORage Manager
CERN	Conseil Européen pour la Recherche Nucléaire
CINT	C++ interpreter
CT board	Control and Transfer board
DCA	Distance of Closest Approach
DST	Data Summary Tape
FEC	Front-End Card
GEANT	GEometry ANd Tracking
GSW	Glashow-Salam-Weinberg theory (of electroweak interaction)
GUT	Grand Unified Theory
JINR	Joint Institute for Nuclear Research, Dubna, Russia
LEP	Large Electron Positron Collider
LHC	Large Hadron Collider
LSF	Load Sharing Facility
MC	Monte Carlo, synonym for random number generators
MTPC	Main TPC
MWPC	Multi-Wire Proportional Chamber

PAW	Physics Analysis Workstation
pQCD	perturbative QCD
PS	Proton Synchrotron
QCD	Quantum-Chromodynamics
QED	Quantum-Electrodynamics
QGP	Quark-Gluon Plasma
RHIC	Relativistiv Heavy Ion Collider, BNL, USA
SLC3	Scientific Linux CERN 3
SPS	Super Proton Synchrotron
TOF	Time Of Flight
TPC	Time Projection Chamber
VTPC	Vertex TPC (within magnets)

Bibliography

[1] D. P. Roy. *Basic constituents of matter and their interactions: A progress report.* hep-ph/9912523, 1999.

[2] Michael Schmelling. *Status of the strong coupling constant.* hep-ex/9701002, 1996.

[3] `http://newstate-matter.web.cern.ch/newstate-matter/`.

[4] Z. Fodor and S. D. Katz. *Critical point of QCD at finite T and mu, lattice results for physical quark masses.* JHEP 04, 050, 2004.

[5] S. A. Bass, M. Gyulassy, Horst Stoecker, and W. Greiner. *Signatures of quark-gluon-plasma formation in high energy heavy-ion collisions: A critical review.* J. Phys. G25 R1-R57, 1999.

[6] Helmut Satz. *The SPS heavy ion programme.* Phys. Rept. 403-404, 33-50, 2004.

[7] R. J. Fries. *Recombination models.* J. Phys. G30 S853-S860, 2004.

[8] The STAR and STAR-RICH collaborations. *Measurements of identified particles at intermediate transverse momentum in the STAR experiment from Au + Au collisions at s(NN)**(1/2) = 200-GeV.* nucl-ex/0601042, 2006.

[9] David d'Enterria. *Indications of suppressed high p(T) hadron production in nucleus nucleus collisions at CERN-SPS.* Phys. Lett. B596, 32-43, 2004.

[10] C. Alt et al. [NA49 collaboration]. *High p(T) spectra of identified particles produced in Pb + Pb collisions at 158-GeV/nucleon beam energy.* nucl-ex/0510054, 2005.

[11] S. Afanasev et al. [NA49 collaboration]. *The NA49 large acceptance hadron detector.* Nucl. Instrum. Meth. A430, 210-244, 1999.

[12] H. Haseroth. *The CERN heavy ion facility.* Invited Paper at the 4th EPAC - European Particle Accelerator Conference - Europhysics Conference, London, UK, 27 Jun - 1 Jul 1994.

[13] G. Brianti. *The CERN Synchrotrons.* CERN 97-04, 1997.

[14] The PS Staff, CERN. *40 years of CERN's Proton Synchrotron. CERN Courier*, 39(10), 1999.

[15] J. Dainton et al. [The CERN SPS and PS Committee]. *Fixed-Target Physiscs at CERN beyond 2005, Summary and Conclusions of an Evaluation by the SPSC.* CERN–SPSC–2005–010, SPSC–M–730, 2005.

[16] N. Antoniou et al. *Letter of intent: Study of Hadron Production in Collisions of Protons and Nuclei at the CERN SPS.* CERN-SPSC-2006-001 and SPSC-P-329, 2006.

[17] Marek Gazdzicki. *Onset of deconfinement and critical point: Future ion program at the CERN SPS.* nucl-ex/0512034, 2005.

[18] The NA60 Collaboration. *NA60 status report.* CERN–SPSC–2005–014, SPSC–M–731, 2005.

[19] Marco van Leeuwen. *Kaon and open charm production in central lead-lead collisions at the CERN SPS.* PhD thesis, Universiteit Utrecht, 2003.

[20] P. Dinkelaker. *ϕ-Produktion in zentralen Blei-Blei-Kollisionen bei 158 AGeV.* Diploma thesis, Johann Wolfgang Goethe-Universität Frankfurt am Main, 2002.

[21] C. Alt et al. [NA49 collaboration]. *Elliptic flow of Lambda hyperons in Pb + Pb collisions at 158-AGeV.* nucl-ex/0510067, 2005.

[22] C. Alt et al. [NA49 collaboration]. *Omega- and Antiomega+ production in central Pb + Pb collisions at 40-A-GeV and 158-A-GeV.* Phys. Rev. Lett. 94, 192301, 2005.

[23] J.-P. Baud et al. *CASTOR status and Evolution.* Paper presented at the International Conference on Computing in High Energy and Nuclear Physics (CHEP), 2003.

[24] O. Bärring et al. *CASTOR: Operational Issues and New Developments.* Paper presented at the International Conference on Computing in High Energy and Nuclear Physics (CHEP), 2004.

[25] `http://consult.cern.ch/service/afs/`.

[26] R. Zybert and P. Bunčić. *DSPACK - Object Oriented Data Manager for HEP.* Paper presented at the International Conference on Computing in High Energy and Nuclear Physics (CHEP), 1995.

[27] Christina Markert. *Lambda (1520)-Produktion in Proton-Proton- und zentralen Blei-Blei-Reaktionen bei 158 GeV pro Nukleon.* PhD thesis, Johann Wolfgang Goethe-Universität Frankfurt am Main, 2001.

[28] Detlef Irmscher. *Philosophy and parts of the global tracking chain.* NA49 Note number 131, 1997.

[29] Frank Eckhardt. *Entwicklung und Bau eines Flugzeitdetektors zur Untersuchung der Hadronenemission in Pb+Pb Reaktionen bei 158 GeV/u Strahlenergie.* PhD thesis, Philipps-Universität Marburg, 1996.

[30] Christof Roland. *Flavor Fluctuations in Central Pb+Pb Collisions at 158 GeV/Nucleon.* PhD thesis, Johann Wolfgang Goethe-Universität Frankfurt am Main, 1999.

[31] Lee Stuart Barnby. *Measurements of* Λ, $\overline{\Lambda}$ *and* K^0_S *from Pb-Pb Collisions at 158 GeV per nucleon in a Large Acceptance Experiment.* PhD thesis, University of Birmingham, 1999.

[32] André Mischke. Λ *und* $\overline{\Lambda}$ *Produktion in zentralen Blei-Blei-Kollisionen bei 40, 80 und 158 GeV pro Nukleon.* PhD thesis, Johann Wolfgang Goethe-Universität Frankfurt am Main, 2002.

[33] Agnes Richard. Λ *und* $\overline{\Lambda}$*-Produktion in zentralen Blei-Blei Kollisionen bei 20 und 30 AGeV am CERN-SPS.* Diploma thesis, Johann Wolfgang Goethe-Universität Frankfurt am Main, 2004.

[34] S. Eidelman et al. [Particle Data Group]. *Review of particle physics.* Phys. Lett. B592, 1, 2004.

[35] R. Brun and F. Rademakers. *ROOT: An object oriented data analysis framework. Nucl. Instrum. Meth.*, A389:81–86, 1997.

[36] `http://root.cern.ch/`.

[37] `http://na49info.cern.ch/na49/Software/minidst/`.

[38] Application Software Group, Computing and Networks Division, CERN. *GEANT – Detector Description and Simulation Tool*. CERN Program Library Long Writeup W5013, 1994.

[39] Milton Toy. *Baryon Stopping and Charged Particle Production from Lead-Lead Collisions at 158 GeV per Nucleon*. PhD thesis, University of California Los Angeles, 1999.

[40] Glenn Cooper. *Baryon Stopping and Hadronic Spectra in Pb-Pb Collisions at 158 GeV/nucleon*. PhD thesis, University of California Berkeley, 2000.

[41] András László. NA49 collaboration internal communication, 2006.

[42] S.V. Afanasiev et al. [NA49 collaboration]. *Energy dependence of pion and kaon production in central Pb + Pb collisions*. Phys. Rev. C66, 054902, 2002.

[43] P. Dinkelaker. *System size dependence of pi,K production at 40A, 158A GeV*. PhD thesis in preparation, 2006.

[44] T. Anticic et al. [NA49 collaboration]. *Lambda and anti-Lambda production in central Pb Pb collisions at 40-AGeV, 80-AGeV, and 158-AGeV*. Phys. Rev. Lett. 93, 022302, 2004.

[45] B. Lungwitz. *Delta Electrons and multiplicity fluctuations*. NA49 Note number 315, 2005.

[46] F. Retiere and M.A. Lisa. *Observable implications of geometrical and dynamical aspects of freeze-out in heavy ion collisions*. Phys. Rev. C70, 044907, 2004.